A STUDY OF MECHANISMS TO ENGINEER FINE SCALE ALPHA PHASE

PRECIPITATION IN BETA TITANIUM ALLOY, BETA 21S

Amit Kishan Behera

Thesis Prepared for the Degree of

MASTER OF SCIENCE

UNIVERSITY OF NORTH TEXAS

August 2013

APPROVED:

Rajarshi Banerjee, Major Professor
Peter Collins, Committee Member
Marcus Young, Committee Member
Narendra Dahotre, Chair of the Department of
        Materials Science and Engineering
Costas Tsatsoulis, Dean of the College of
        Engineering
Mark Wardell, Dean of the Toulouse Graduate
        School

Behera, Amit Kishan. *A Study of Mechanisms to Engineer Fine Scale Alpha Phase Precipitation in Beta Titanium Alloy, Beta 21S.* Master of Science (Materials Science and Engineering), August 2013, 78 pp., 1 table, 39 figures, references, 44 titles.

Metastable β-Ti alloys are titanium alloys with sufficient β stabilizer alloying additions such that it's possible to retain single β phase at room temperature. These alloys are of great advantage compared to α/β alloys since they are easily cold rolled, strip produced and can attain excellent mechanical properties upon age hardening. Beta 21S, a relatively new β titanium alloy in addition to these general advantages is known to possess excellent oxidation and corrosion resistance at elevated temperatures. A homogeneous distribution of fine sized α precipitates in the parent β matrix is known to provide good combination of strength, ductility and fracture toughness. The current work focuses on a study of different mechanisms to engineer homogeneously distributed fine sized α precipitates in the β matrix. The precipitation of metastable phases upon low temperature aging and their influence on α precipitation is studied in detail. The precipitation sequence on direct aging above the ω solvus temperature is also assessed. The structural and compositional evolution of precipitate phase is determined using multiple characterization tools. The possibility of occurrence of other non-classical precipitation mechanisms that do not require heterogeneous nucleation sites are also analyzed. Lastly, the influence of interstitial element, oxygen on α precipitation during the oxidation of Beta 21S has been determined. The ingress of oxygen and its influence on microstructure have also been correlated to measured mechanical properties.

ACKNOWLEDGEMENTS

TABLE OF CONTENTS

LIST OF TABLES

LIST OF FIGURES

CHAPTER 1

INTRODUCTION

1.1.Titanium and Its Alloys

Titanium, named after the Titans of Greek mythology, was identified as a new metallic element in England in 1791. The high reactivity of titanium with oxygen and nitrogen made it impossible to obtain pure titanium until the development of 'Kroll process' in middle of 20th century [1]. The process involves the reduction of titanium tetrachloride ($TiCl_4$) with magnesium in an inert gas atmosphere. Titanium alloys are most useful owing to their good combination of strength, toughness, ductility, and corrosion resistance.

1.1.1 Phases and Phase Transformations

The combined influence of many factors such as temperature, pressure, and alloying additions leads to the existence of a number of different equilibrium and non-equilibrium phases in titanium alloys. The presence of a particular phase is dominated by thermodynamics based lowest free energy criteria when steady state conditions are maintained. However, under non-steady state scenarios, the kinetics of transformation can dominate resulting in the formation of different metastable phases.

The common equilibrium and non-equilibrium phases of titanium are

i.   Alpha phase (α): The most common low temperature stable phase found in pure titanium and its alloys. It has a hexagonal closed packed (HCP) structure with a space group of $P6_3mmc$.

ii. Beta phase (β): A high temperature phase, which occurs at temperatures above $882\pm2^{o}C$ for pure titanium. The addition of β stabilizing elements decreases this

temperature and also provides a range of temperature for the coexistence of α and β phases. It has a body centered cubic (BCC) structure with space group of Im-3m.

iii. Martensitic phases: Two types of non-equilibrium martensitic phases are found in titanium systems; α' and α''. α' is formed during extreme fast quenching from the high temperature β phase. Its crystal structure is hexagonal (P6$_3$mmc). α'' is also formed by martensitic transformation; however it has a higher solute content compared to α'. In addition to fast quenching methods, α'' can also form during application of stress (stress induced or strain induced transformation).

iv. Omega phase (ω): Omega phase in titanium alloys is a metastable phase that is commonly seen as a transition phase of β to α transformation. It is by far the most studied metastable phase in these systems and its role in α precipitation has been examined in great detail. The structure of ω phase can be either hexagonal or trigonal depending on the extent of completion of the transformation.

Titanium and its alloys are found to undergo an array of solid state phase transformations, especially when they undergo different thermo-mechanical treatments. A combination of these phase transformations is usually necessary for optimizing the mechanical properties of the material.

Different commonly found phase transformations are

i. Diffusional transformation (β −> α): The diffusional transformation leading to α nucleation and growth is the most important transformation in titanium alloys due to its effect on mechanical properties. This transformation decides the morphology, distribution, size scale and volume fraction of α precipitates in the β matrix, which can significantly influence the final properties of the material. The different

heterogeneous nucleation sites that can assist α precipitation are; grain boundaries, intragranular defects, metastable phases (α", ω), β phase separated regions [2].

ii. Shear transformations (β –> α',α") : The formation of α' and α" is by a martensitic transformation where the transformation is not thermally activated and happens at speeds almost close to that of sound [3]. This occurs during the fast quenching of single β phase to room temperature or under application of stress, in case of α" precipitation.

iii. Shuffle transformation (β –> ω): The ω phase formed in β matrix is classified into athermal ω and isothermal ω types. The athermal ω are supposed to form by a diffusionless, purely displacive collapse of the {111} planes of the β phase via a shuffle mechanism[4]. The isothermal precipitates were postulated to form by a thermally activated process involving diffusion based compositional partitioning. The regions depleted with ω destabilizing elements then formed ω phase by collapse of the {111} bcc planes[4], [5]. Athermal α" results from a pure structural instability whereas isothermal ω results from concurrent compositional and structural instabilities.

iv. Phase separation of β (β–>β$_1$+β$_2$) : A phase separation reaction in the beta matrix leads to the formation of two regions, one being rich and other being lean in β stabilizers [2]. The two regions have the same crystal structure as the parent matrix but different values of lattice parameter due to their different compositions.

1.1.2   Classification of Its Alloys

Commercial titanium alloys are classified into different categories based on their equilibrium constitution. This can be ascertained based on their position in a pseudo-binary section through a beta isomorphous phase diagram as shown in Figure 1.

3

i. Alpha (α) alloys: Pure titanium and its alloys having only alpha stabilizers that are stable with hcp (α) structure at room temperature are categorized as alpha (α) alloys. These alloys are generally non heat treatable but possess good strength and toughness levels along with good oxidation resistance [6].

ii. Alpha + beta (α+β) alloys: The range of (α+β) alloys extends from the α/(α+β) phase boundary till the point of intersection of Ms curve with the room temperature (RT) line in the pseudo-binary section of the beta isomorphous phase diagram. These alloys, under no circumstances could retain a single β phase at room temperature. Commercial α+β alloys possess a two phase (α+β) microstructure that provides a combination of high strength of α alloys and good ductility of β alloys.

iii. Metastable beta (β) alloys and β alloys: These are alloys for which it is possible to retain β phase at room temperature. Their range extends beyond the point of intersection of the Ms curve with the room temperature line in Figure 1. The addition of sufficient β stabilizing alloying elements ensures that the formation of martensitic phases is not feasible. These alloys are usually heat treated in the (α+β) phase field to produce a bimodal phase mixture that provides the desired value of mechanical and other properties.
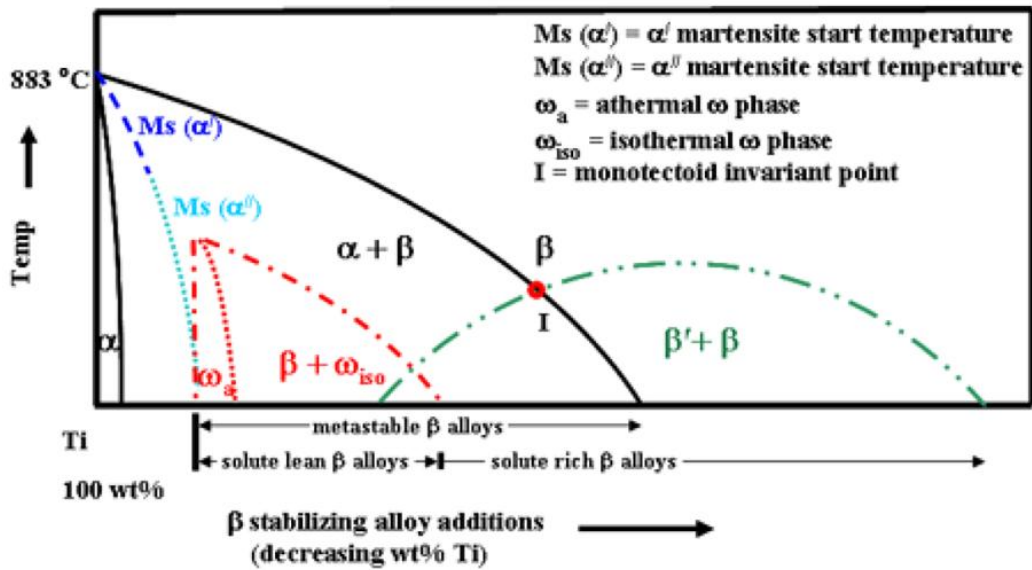
Figure 1: Pseudo binary section through a beta isomorphous phase diagram [7]

1.2. Beta Titanium Alloys and Their Applications

As discussed earlier, it is possible in β-Ti alloys to retain a single β phase upon rapid cooling to room temperature. These alloys can be heat treated to obtain high strength values (in excess of 1400Mpa). They are easily cold rolled and are known for their good formability and weldability [2]. The properties can be varied along a large range depending upon the wide scale of possible heat treatments for these alloys. Beta titanium (β-Ti) alloys can also be classified into a) solute rich and b) solute lean alloys. The solute lean alloys tend to decompose easily as compared to the solute rich ones.

Some of the commonly found β-Ti alloys are Ti-10V-2Fe-3Al (Ti-10-2-3), Ti-15V-3Cr-3Al-3Sn (Ti-15-3), Ti-11.5Mo-6Zr-4.5Sn (Beta III), Ti-5Al-5Mo-5V-3Cr-0.5Fe (Ti5553) and Ti-15Mo-2.7Nb-3Al-0.3Si (Beta 21S). The use of these alloys has been on gradual increase in recent times. The first noteworthy application of beta alloys happened in the early 1990s in the Boeing 777 aircraft. High strength forgings made of Ti-10V-2Fe-3Al were used extensively in the landing gear structure [8]. The Boeing 777 also used Ti-15V-3Cr-3Al-3Sn sheet in environmental control and floor support applications. New

developments are being made to use β-Ti alloys as high strength fasteners. Damage tolerant applications are also actively explored owing to the improved fracture toughness and fatigue properties of new generation β-Ti alloys.

The discovery and use of Beta 21S alloy was a major breakthrough with respect to high temperature application of β-Ti alloys. β-21S was found to be able to overcome the general shortcomings of β-Ti alloys, which ordinarily have poor creep and oxidation resistance [9]. Additionally, β-21S is identified as the only β-Ti alloy to be resistant to attack by thermally decomposed hydraulic acid [9]. This makes it highly applicable in exhaust nozzles of aircraft engines.

1.3. Goals of the Present Study

β-Ti alloys are capable of being heat treated over a broad range of strengths, in order to provide the desired combination of strength and fracture toughness. The present study intends to understand the different possible heat treatment procedures that would result in such desired microstructures. In most cases, a homogeneous distribution of fine sized precipitates in the parent matrix gives good combination of strength and fracture toughness. Thus the focus of the work is to determine various possible heating cycles that would result in fine size scale alpha precipitation. The role of metastable intermediate phases, interstitial additions on precipitate nucleation is studied extensively. The possibility of homogeneous precipitation directly from the beta matrix without help of heterogeneous nucleation sites is also investigated.

The primary goals and corresponding studies have been categorized into 3 broad sections

    i.   Studies to understand the influence of low temperature aging on α precipitation

a) The precipitation behavior on two step aging showcasing the possible role of intermediate metastable phases

b) Precipitation behavior upon prolonged isothermal aging below ω solvus temperature and influence of increasing density of metastable phases on α precipitation

c) Precipitation behavior upon continued isothermal aging above ω solvus temp

ii. Examine the possibility of homogenous α precipitation directly from β matrix without the aid of heterogeneous nucleation sites

iii. Investigate the effect of oxygen on alpha precipitation and consequently mechanical properties during the oxidation of Beta 21S alloy

CHAPTER 2

EXPERIMENTAL DETAILS

The current section discusses about the material system that has been the used to study the relevant mechanisms for fine scale alpha precipitation in the beta matrix of titanium alloys. The applications and advantages of the particular alloy system, Beta 21S has also been described. The experimental techniques and tools used for the heat treatment, characterization and mechanical testing of the material have been discussed briefly.

2.1.Materials Alloy/System

Timetal 21s (or more commonly known as Beta 21S) is a metastable β-Ti alloy developed by the company TIMET USA, which is similar to Ti-15-3 but has improved oxidation and corrosion resistance [9]. The nominal chemical composition of the alloy is given by Ti-15Mo-2.7Nb-3.0Al-0.2Si (in weight percent) [10]. The material for the current study was received directly from TIMET in the form of cold rolled and subsequently beta annealed sheets of approximately 1 mm thickness. The beta transus temperature of the material is known to be around 807^oC. Other important physical properties for the alloy are listed in Table 1 [10].

Table 1: Beta 21S, Physical properties [10]

Property	T (^{o}C)	Value (SI units)
Beta transus	807	-
Density	22 (RT)	4.93gm.cm^{-3}
Thermal conductivity	33	7.6 Wm^{-1}K^{-1}
Electrical resistivity	24 (RT)	1.35 $\mu\Omega$.m
Specific heat capacity	24 (RT)	0.117 JKg^{-1}K^{-1}
Mean coefficient of thermal expansion	24 (RT)	7.06 x10^{-6} mm^{-1o}C^{-1}
Modulus of elasticity (solution treated)	24 (RT)	72-85 GPa

Metastable beta titanium alloys are generally easily heat treatable, highly formable and capable of high strength upon adequate heat treatment. Timetal 21S also shows these qualities and is thereby easily cold rollable, strip producible, age hardenable [11]. It is known to retain its strength at relatively high temperatures unlike most other beta titanium alloys. Additionally, it also possesses good oxidation and corrosion resistance which makes it very suitable for high temperature applications. It is readily used in plug and nozzle applications in commercial aircraft engines due to its resistant to hot hydraulic fluids such as Skydrol.[9]

2.2.Heat Treatments

Heat treatments for all experiments were carried out in tube furnaces or box furnaces with K-type thermocouple attachments. Heat treatments at temperatures above $400^{o}C$ were done in an atmosphere of argon gas to prevent oxidation of the samples. However, for temperatures less than $400^{o}C$, samples were just wrapped in pure titanium foils to minimize surface oxidation. In some cases, after the aging treatment, samples were water quenched to get the required fast cooling rates. The samples were rapidly pulled out of the furnace and directly dropped into a bucket of water kept nearby. For cases of slower cooling rates, air cooling was done with the samples being simply left alone in air to cool down.

In experiments that required step quenching from one temperature to another, a set-up of two adjacently placed tube furnaces was used. The two furnaces were initially pre-heated to desired temperatures. The samples were then wrapped in titanium foils (or were placed in atmosphere of argon gas) and placed on a ceramic boat inside the first furnace. Upon completion of heating at the first temperature, the samples were pushed using ceramic push-rods into the second furnace. The process took very less time, usually less than 5 seconds and hence followed quite closely the desired heating cycle.

Oxidation experiments were done in an open box furnace, which was pre-heated to the desired temperatures. The samples were placed on their edges on ceramic plates to ensure maximum surface area exposure to the atmosphere.

2.3.Characterization Tools

2.3.1. Scanning Electron Microscope

In most cases investigations regarding the evolved α/β microstructure were done using SEM. The most frequently used equipment was the FEI Sirion™ FEG instrument operating at 15-30 keV. The instrument was equipped with a Field emission gun (FEG), back scattered electron detector (BSE), Everhart-Thornley secondary electron (SE) detector and through the lens (TLD) detector. The instrument also had an energy dispersive spectrometer (EDS) attached to it for chemical composition measurements. An electron back scattered diffraction (EBSD) system was also fitted into the instrument that enabled orientation related studies to be done using the equipment. Different modes of imaging used included secondary electron mode, back scattered electron mode and immersion mode. Immersion mode was specifically very useful in obtaining micrographs at very high magnifications.

2.3.2. Focused Ion Beam

The FEI DualBeam (FIB-SEM) (Nova Nanolab 200™) system was used as a sample preparation tool to make site specific specimens for transmission electron microscopy or 3D atom probe studies. In the instrument, gallium ions are accelerated and focused onto specific regions in the sample to preferentially mill out regions of interest. Once the desired specimen is prepared by milling its surrounding areas, it is lifted out in-situ with help of an Omniprobe manipulator, attached to the instrument.

TEM samples are prepared by attaching this lift-out specimen, usually in form of rectangular blocks, to a copper grid that would be inserted in the microscope. After attaching the specimen to the copper grid, it is sequentially milled to a thickness of electron transparency. Different voltage and current values are used for the gallium ions to minimize beam damage suffered by the sample. A protective coating of platinum is usually put on top of the sample at the start to reduce the damage to the region of interest.

Specimens for 3D atom probe are prepared in a slightly different manner compared to TEM sample preparation. FIB is used to prepare atomically sharp tips (tip radius less than 100nm) that could be analyzed using the 3DAP. These sharp tips are prepared by first placing rectangular blocks of the sample on top of pillars made out of silicon. These pillars are themselves quite sharp with a flat circular base on their top. These blocks are then milled using concentric circles of milling to eventually take the shape of cones with very sharp tip radius. Further details regarding the sample preparation procedure for APT studies is available in published literature [12].

2.3.3. Transmission Electron Microscope

In cases, where the size of alpha precipitates or metastable intermediate phases were too small to be characterized using the SEM, transmission electron microscopy was needed to identify and study the characteristics of the phases. The specimens were analyzed using a FEI Tecnai F20™-FEG instrument. The instrument also had a scanning transmission electron microscopy (STEM) detector for 'z' contrast imaging and STEM-EDS detector for chemical composition measurements.

2.3.4. Three Dimensional Atom Probe

Three dimensional (3D) atom probe (3DAP) is a micro-analytical technique that is used for near atomic resolution determination of the elemental identities and spatial

coordinates of individual atoms within a small volume [13]. The technique uses voltage pulses or laser beam to pull out atoms in form of ions from very sharp specimen tips and then provide a 3D reconstruction of the entire evaporated volume. The chemical identification of ions is based on their measured time of flight from the specimen tip to the detector. The time of flight for different ions varies with their mass to charge ratio. The spatial coordinates of the ion are determined by the encoded impact position on the position sensitive detector. A detailed analysis of the working of 3DAP and its contribution in scientific understanding is given elsewhere [13], [14]

2.4. Mechanical Testing

2.4.1. Micro-Hardness

A dynamic ultra micro hardness tester (DUH-211S) from Shimadzu Scientific Instruments was used to perform hardness measurements on samples aged at different conditions. The instrument uniquely measures the dynamic indentation depth in addition to the indentation dimensions after the test. It provides two separate readings, one based on its depth sensor and the other using conventional indentation size measurements by the operator. It also provides the load versus depth curve for the entire testing cycle. The elastic modulus of the material can be calculated based on the slope of load versus depth curve during the unloading cycle.

2.4.2. Nano-Indentation

In scenarios where measurements were needed to be made at much smaller size scale than possible using a micro-harness tester, nano indentation technique was utilized. In this technique, an indenter with a geometry known to high precision (a Berkovich tip, with a three

sided pyramid geometry) is used. During the indentation process, the depth of penetration is noted and is used to calculate the area of the indentation. Different mechanical properties are calculated using the plotted graph between load and displacement (depth).

CHAPTER 3

INFLUENCE OF TWO STEP AGING HEAT TREATMENT ON

FINE SCALE α PRECIPITATION

3.1. Introduction and Motivation

The role of metastable phases to influence precipitation behavior of thermodynamically stable phases, as discussed earlier, is fast developing as a useful mechanism to tailor final microstructures for practical application requirements. The current chapter deals with identification of the possible role of metastable phases (omega phase) on the nucleation behavior of stable alpha phase. The study deals with precipitation of these metastable and stable phases in commercially available β-Ti alloy, Beta 21S. Beta 21S is an unique and important β-Ti alloy with excellent high temperature oxidation, corrosion resistance, and creep behavior. However, studies regarding the influence of low temperature metastable phases on precipitation of stable phase have not been pursued in great detail.

In the present work, conventional microscopy techniques have been used to identify the precipitation of athermal and isothermal omega phase in Beta 21S alloy. The precipitation of alpha phase with possible assistance from these metastable phases is also investigated. Atom probe tomography technique has been used to determine the compositional evolution of the metastable omega phase and the alpha phase. High energy X-Ray diffraction studies have been carried out to establish the presence or growth/dissolution of the different constituting phases upon heat treatment. The combined understanding developed by combining the above techniques sheds light on the possible role of omega phase in alpha precipitation and its characteristic features.

3.2. Background and Previous Literature

The precipitation of omega phase and its possible influence on alpha precipitation have been the subject of investigation for various researchers over the years [15], [16]. Recently, extensive analysis on the precipitation sequence in commercial Ti-5553 β-Ti alloy has been performed by S. Nag et al. [17]. Studies on alpha-nanophase nucleation from omega particles using high resolution microscopy has been carried out by Prima et al. on low cost beta titanium alloy (LCB) [18].

The formation of omega phase could happen due to its athermal precipitation during fast quenching experiments from single beta phase or due to isothermal precipitation during low temperature aging heat treatments. Over the years, different mechanisms have been proposed to explain the role of omega precipitates on nucleation of alpha phase. However, these mechanisms listed below are found to explain observations related to specific alloy systems:

i. In Ti alloy systems with large misfit between the omega and beta phases, alpha precipitates have been shown to nucleate on ledge and misfit dislocations at the omega/beta interface [19]. The large misfit tends to give a cuboidal shape to these omega precipitates. These precipitates upon coarsening lose coherency with beta phase, making them potent sites for alpha nucleation. Such behavior is generally observed for Ti-V alloy systems [15].

ii. In other alloy systems with lower mismatch between omega and beta phases, such as Ti-Mo system, the precipitates are seen with a spherical/ellipsoidal shape. The behavior of the omega phase in such systems is not clearly understood. Previous studies on Ti-15wt% Mo alloy by Pennock et al. [20] reported possible omega assisted nucleation of alpha precipitates during a two-step aging process, after quenching from temperature above the

beta solutionizing temperature. The results also suggested an influence of heating rate on the role of the omega phase in nucleating alpha precipitates.

In spite of being the subject of investigation for many years, there is still no single confirmed theory about the role of omega precipitates in alpha nucleation in low omega/beta misfit alloys. Different schools of thought regarding the mechanism for the same are as follows:

a. Studies performed by Azimzadeh and Rack [21] on low cost beta (LCB) titanium alloy indicate alpha precipitate nucleating near, but at a certain distance from the omega/beta interface. The local enrichment of Al near the omega/beta interface, which is an alpha stabilizer along with being an omega destabilizer, helps in the nucleation of alpha precipitates. Atom probe results showing such local enrichments have also been reported in literature [16].

b. Recent studies by Prima et al. on LCB titanium alloy [18], [22] have shown the nucleation of alpha platelets within the core of omega precipitates. Dark field TEM and HRTEM results show plate like morphology of nano phase alpha. These have been suggested to nucleate mainly by a displacive mechanism in the core of isothermal omega precipitates.

3.3. Experimental Procedure

The material used for the current investigation was obtained in the form of rolled sheets from TIMET company. The alloy was cold rolled to its final thickness prior to being annealed at a temperature above its beta transus temperature. The as-received microstructure was believed to consist of single phase beta; however, subsequent analysis showed it to contain a small volume fraction of omega precipitates in the beta matrix. The starting microstructural condition for all experiments was achieved by beta solutionizing the as-

received samples at 900°C for 30mins and subsequently water quenching them to room temperature. The starting microstructure consisted of beta phase with a minor amount of athermal omega precipitates as shown in later sections. All subsequent heat treatments were done by placing the samples in pre-heated furnaces set to desired temperatures.

Similar procedures, as mentioned in section 2, were followed for specimen preparation to be analyzed using different characterization techniques i.e. SEM, TEM, 3DAP etc. SEM was used to study the precipitation characteristics of alpha phase that included its size scale, morphology, nucleation density, and volume fraction. TEM studies helped in identification and observation of precipitates at a much smaller size scale or at early stages of precipitation. Local electron atom probe (LEAP) studies enabled accurate compositional measurement of various constituting phases and the partitioning of alloying additions among these phases. In addition to these techniques, high resolution x-ray diffraction studies using synchrotron based radiations were performed to study the phase evolution in accordance with different heat treatments. The use of a gleeble set up along with the synchrotron facilities enabled diffraction data to be collected in situ during the annealing heat treatments.

The influence of omega precipitates on alpha precipitation was studied using two different heat treatment cycles, shown schematically in Figure 2 ;

   i. Extended isothermal annealing at specified temperatures (350°C, 400°C)

   ii. Two step annealing process, with low temperature annealing (at 350°C, 400°C) followed by high temperature aging (at 600°C).

The two aging temperatures (350°C and 400°C) chosen above are assumed to lie on either side of the omega solvus temperature for Beta21s alloy based on previous studies [11]. The results shown below have been organized to analyze the effect of omega phase on alpha precipitation when the alloy is isothermally held at above and below the omega solvus

17

temperature. The effect of omega phase on alpha precipitation is studied for cases involving long term isothermal annealing and also two-step annealing heat treatments.
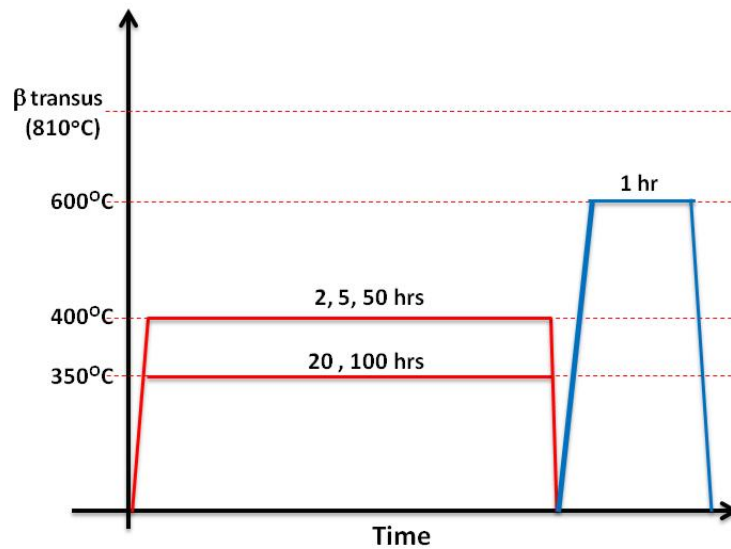
Figure 2: Heat treatment schedules

3.4. Results and Discussions

The current study aimed at understanding the possible role (if any) of metastable omega phase on the nucleation of alpha phase and comparing it with other possible nucleation mechanisms. The starting alloy condition for all experiments was kept identical, with the alloy being solutionized above beta transus temperature and subsequently water quenched to room temperature. This ensured that the starting microstructure for all experiments was arguably pure single beta phase.

SEM micrographs of the water quenched samples show single phase beta microstructure, with average beta grain size of 80-100 microns, as shown in Figure 3. Investigations were also done to examine possible precipitation of omega precipitates in the starting microstructure during water quenching from above beta transus temperature. Diffraction studies using TEM indicated the presence of athermal omega precipitates in the

water quenched samples. In Figure 3(b), a selected area diffraction (SAD) pattern obtained along <113>β zone axis shows reciprocal lattice streaking (RLS) at 1/3 and 2/3 (112)β positions due to omega precipitation. The nucleation density and size scale of these athermal omega precipitates has been discussed in the subsequent analysis.
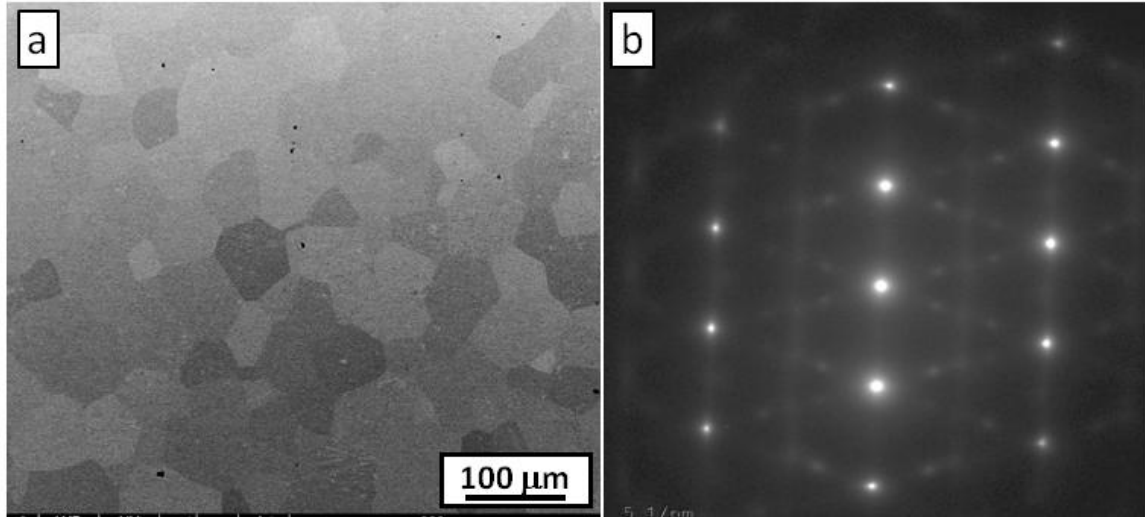
Figure 3: (a) SEM micrograph in BSE mode showing beta grains in starting material, (b) TEM-SAD pattern along β[113] zone axis of starting material

3.4.1. Effect of Isothermal Omega Precipitation on Alpha Nucleation

The precipitation of omega phase is known to possibly influence alpha phase precipitation by the work of many previous researchers [17]. The exact role of it or the process through which it helps alpha precipitation is still not very clear, though numerous mechanisms have been suggested. The omega precipitates are assumed to act as (or provide) heterogeneous nucleation sites for alpha nucleation and thereby increase the nucleation density of alpha precipitates. As omega precipitates are distributed homogenously in the beta matrix, the resulting alpha precipitates are also homogenously distributed in the entire beta matrix. In order to study the role of omega precipitates on alpha nucleation, three sets of heat treatments were designed. In the first case, samples were annealed at 350°C for 5hrs then rapidly heated and isothermally held at 600°C for 1hr followed by fast cooling to room

temperature. The second case was similar to the first, with the initial aging temperature changed to 400°C. The third heat treatment involved direct heating of the samples to 600°C and holding them there for 1 hour, before fast cooling to room temperature. SEM micrographs obtained at the end of all three heat treatments have been shown in Figure 4. Direct aging at 600°C is seen to result in alpha precipitation mainly along the grain boundaries. The minimal intragranular precipitation indicates no significant role of athermal omega precipitates on the nucleation of alpha precipitates. The second heat treatment involving aging at 350°C is seen to have resulted in finer intra-granular alpha precipitation compared to the one aged at 400°C. The results suggest that omega precipitation obtained on aging below the omega solvus temperature has indeed an effect on subsequent alpha precipitation at higher temperatures. The omega precipitates are possibly providing additional heterogeneous nucleation sites for alpha precipitation.
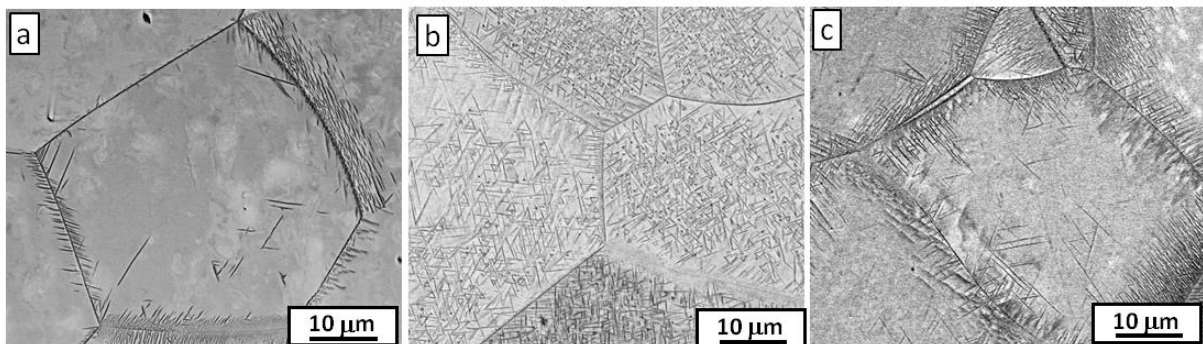
Figure 4: SEM micrographs obtained using BSE mode after different heating treatment (a) directly aged at 600°C for 1 hour (b) 350°C/5hr + 600°C/1hr (c) 400°C/5hr + 600°C/1hr

3.4.2. Microstructure Evolution on Isothermal Annealing Below ω Solvus Temperature

In order to study the temporal evolution of omega precipitates, water quenched Beta 21S samples were subjected to isothermal annealing at 350°C for different time intervals. Chaudhari et al. [11] in their work on Beta 21S alloy have shown the formation of isothermal omega precipitates upon aging at 350°C. Figure 5 shows SAD patterns along [110]β zone

axis taken from samples after aging at 350°C for different times (Fig 3(b) and (c) - aged for 20 and 100hrs respectively). In both cases, intensity maximas corresponding to omega precipitates can be seen at 1/3 and 2/3 {112}β positions. The increase in the relative intensity of these spots with increasing aging time provides evidence for the continuing precipitation of omega precipitates upon isothermal aging at 350°C. The SAD patterns after 20 and 100hrs aging also show faint spots at 1/2{112} positions, suggesting the possibility of slight alpha precipitation during isothermal annealing at 350°C.
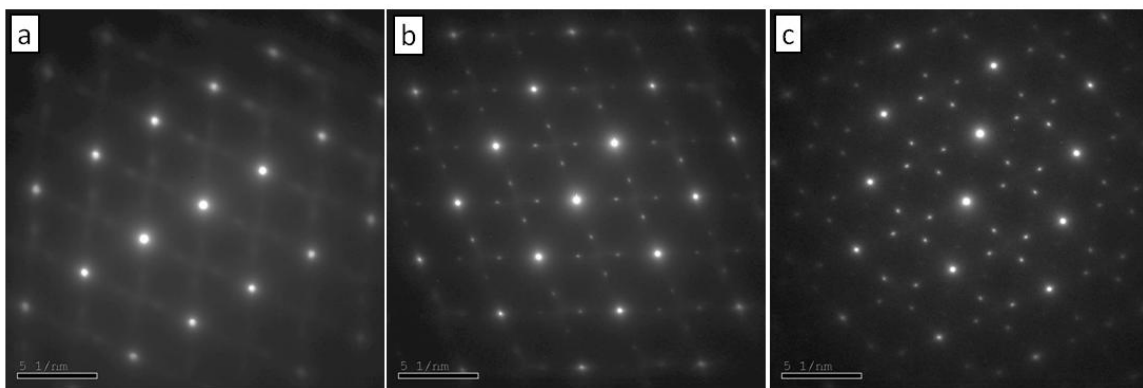
Figure 5: TEM-SAD patterns along [110]β zone axis for (a) starting water quenched material (b) after 20hrs aging at 350°C (c) after 100hrs aging at 350°C

These omega precipitates are seen as bright ellipsoidal spots in the dark field imaging mode using TEM, as shown in Figure 6. The spots correspond to a few selected variants of omega precipitates as the objective aperture was positioned to allow only certain diffracted beams to reach the detector. Figure 6(a) shows the extremely fine sized athermal omega precipitates in the beta solutionized/water quenched sample. After prolonged isothermal aging at 350°C, there is precipitation of relatively larger sized omega precipitates with lesser density as compared to the athermal omega precipitates. However, the size and density of these precipitates increases further with continued aging from 20hrs to 100hrs, as shown in Figure 6(a) and (b) respectively. In a few cases, extremely fine alpha laths are observed to be nucleating close to omega precipitates, though its exact relation cannot be ascertained due to

the two-dimensional limitation of these micrographs. After aging for 100hrs, these alpha laths seemed to have slightly elongated and increased in size, compared to those seen after 20hrs aging.
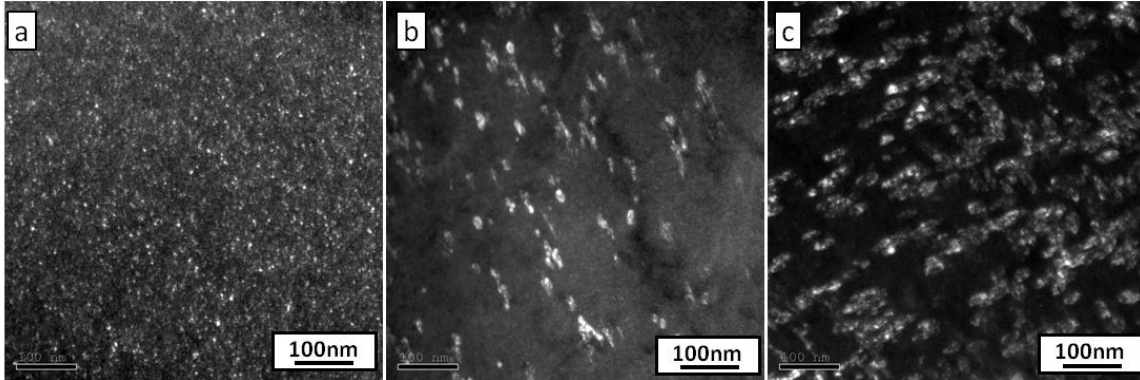
Figure 6: Dark field mode TEM micrographs for samples (a) starting material (b) aged for 20hrs at 350°C (c) aged for 100hrs at 350°C

Dark field imaging is highly useful in identifying the shape and size scale of individual precipitates; however it is difficult to predict the nucleation density as it shows limited variants of the precipitate at one time. Scanning transmission electron microscopy (STEM) based imaging is thereby carried out to determine the increase in nucleation density of omega precipitates upon isothermal annealing. Figure 7(a) and (b) show STEM micrographs recorded from samples that were isothermally aged at 350°C for 20 and 100hrs respectively. The dark ellipsoidal spots correspond to omega precipitates which have lesser average atomic number due to the rejection of the heavier beta stabilizing alloying additions (Mo and Nb). Atom probe based composition measurements, discussed in subsequent sections, shows omega precipitates to be essentially titanium rich pockets with all other alloying additions being rejected from them. The density and size of these dark spots/precipitates can be seen to increase with increase in isothermal aging time.
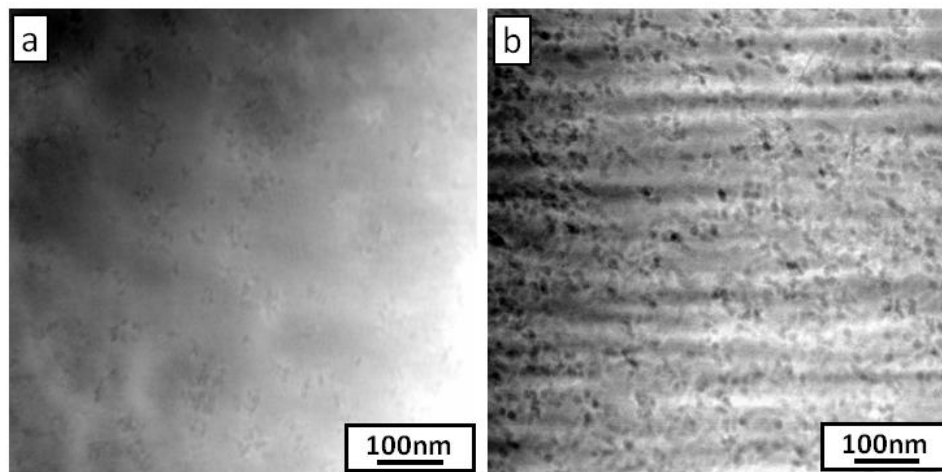
Figure 7: STEM micrographs for samples aged at 350°C for (a) 20hrs (b) 100hrs

The structural nucleation/growth of omega precipitates upon isothermal aging at 350°C is well seen with help of TEM observations. However, in order to study the compositional evolution of these omega precipitates, 3DAP tomography experiments were performed on samples aged at 350°C for 20hrs and 100hrs. The composition of constituting phases at different stages of isothermal annealing was determined. Figure 8 and Figure 9 show results obtained from 3D-APT analysis of samples aged for 20hrs and 100hrs respectively. For the case of 20hrs aging, a complete ion map for the reconstructed volume has been shown in Figure 8(b). The figure shows the omega precipitates enclosed by a user made iso-concentration surface, with 92 at% titanium concentration. Regions enriched with only titanium and depleted of all other alloying additions (Mo, Al) can be seen as pockets in Figure 8(c). Individual constituents have been marked with different colored dots as listed. The shape of the precipitate is clearly seen to be ellipsoidal from these reconstructions. A proximity histogram, showing the compositional variation of individual elements averaged over the entire omega/beta interface, is plotted in Figure 8(a). Omega precipitates are seen to reject all alloying additions, becoming almost pure titanium pockets.

23

Similar APT studies were also carried out on samples aged for 100hrs at 350°C. Figure 9(b) shows a section of the reconstructed tip volume containing multiple omega precipitates. The omega precipitates are enclosed by a user made iso-concentration surface with 92 at% titanium concentration. A 1D composition profile generated along the cylinder shown in Figure 9(b) has been plotted in Figure 9(a). The profile shows 10-12 at% of Mo and 5-7 at% of Al in the beta matrix and less than 1 at% for either Mo or Al in the omega precipitates. The composition of the omega precipitates can be seen to not change much with increase in aging times from 20hrs to 100hrs. A 2D contour map for titanium concentration shown in Figure 9(c) showcases the ellipsoidal titanium rich pockets of omega precipitates.
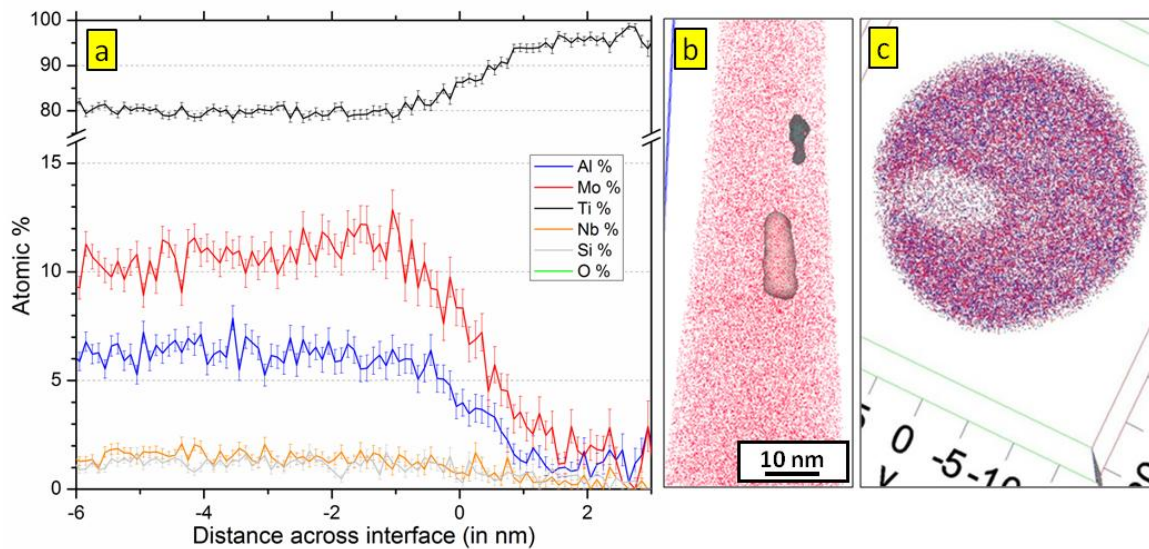
Figure 8: (a) Proximity histogram showing averaged compositional changes across the omega/beta interface, (b) Reconstructed tip volume showing omega precipitates inside red colored Mo atoms, (c) top view showing omega precipitate depleted of Mo (red dots) and Al atoms.
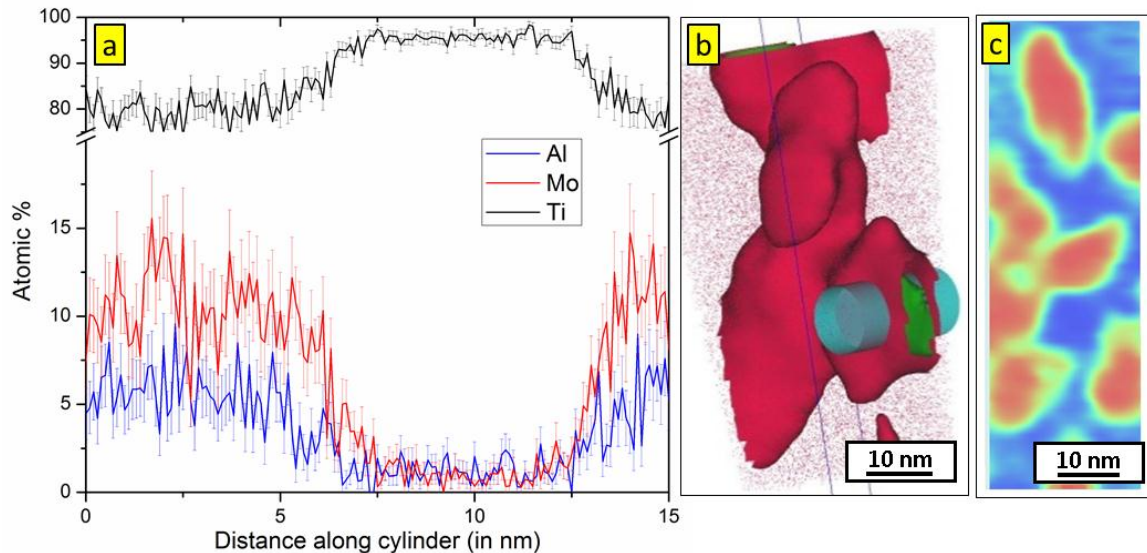
Figure 9: (a) 1Dimensional composition profile showing different in composition of omega and beta phases (b) Iso-concentration surface showing omega precipitate along with cylinder used for 1D composition profile (c) 2D contour map for Ti concentration showing Ti rich omega precipitates

TEM micrographs, obtained in dark field imaging mode for samples aged till 100hrs at $350^{o}C$, could be seen in some cases to have alpha phase nucleating close to the existing omega precipitates. An example of such mutual existence is shown in Figure 10(b). Similar combinations of alpha and omega precipitates have also been captured using APT experiments. A 2-dimensional plot depicting Mo concentration with pseudo colors is plotted using APT analysis in Figure 10(a). The red color corresponds to low concentration of Mo while the blue corresponds to higher concentrations. Omega precipitate in the center could be seen to have minimal Mo content while an alpha precipitate with slightly higher concentration of Mo could be seen growing close to it on its left. The corresponding tip reconstruction containing both alpha and omega precipitates is shown in Figure 11(b). The alpha lath seems to be nucleating close to the omega/beta interface on the left side. Both the alpha lath and omega precipitate are enclosed by an iso-concentration surface of 87 at% titanium. A 1D composition profile calculated from right to left along the cylinder shown in

25

this figure is plotted in Figure 11(a). The center of the cylinder is depleted in both Al and Mo (less than 1 at %), representing omega phase. However, at the left edge of the cylinder, slight increase in Mo (~ 4 at %) and Al (~ 2 at %) content is observed. These measurements assumably represent the starting composition for alpha precipitates growing in close proximity to existing omega precipitates. These regions are also noted to have slightly lower titanium content compared to omega precipitates. These results match previous observations by other researchers [17] who suggest that alpha precipitates nucleate close to the omega/beta interface.
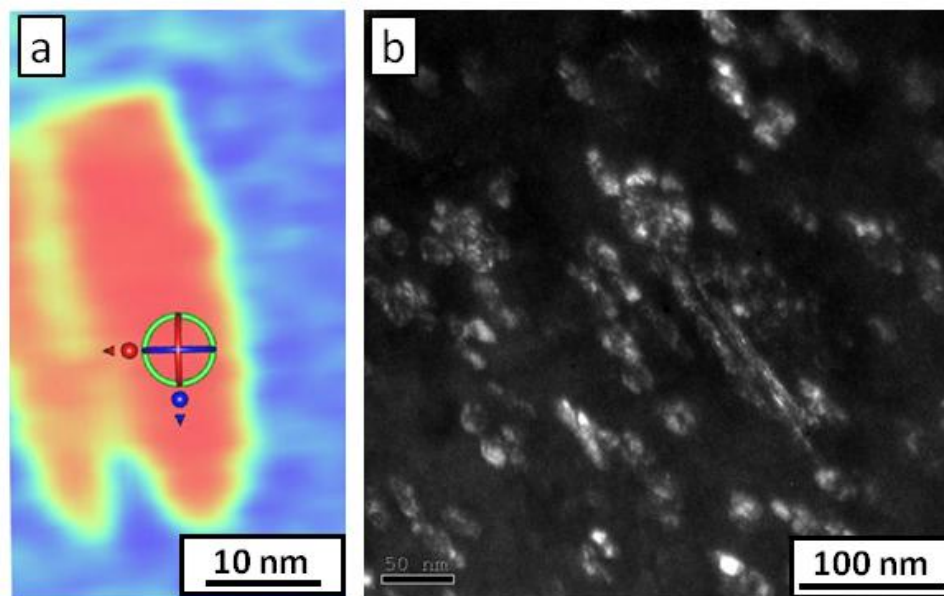
Figure 10: (a) 2D contour plot for Mo concentration (red-low, blue-high) , (b) TEM micrograph using dark field mode showing alpha nucleation close to existing omega precipitates, for samples aged at 350°C for 100hrs,
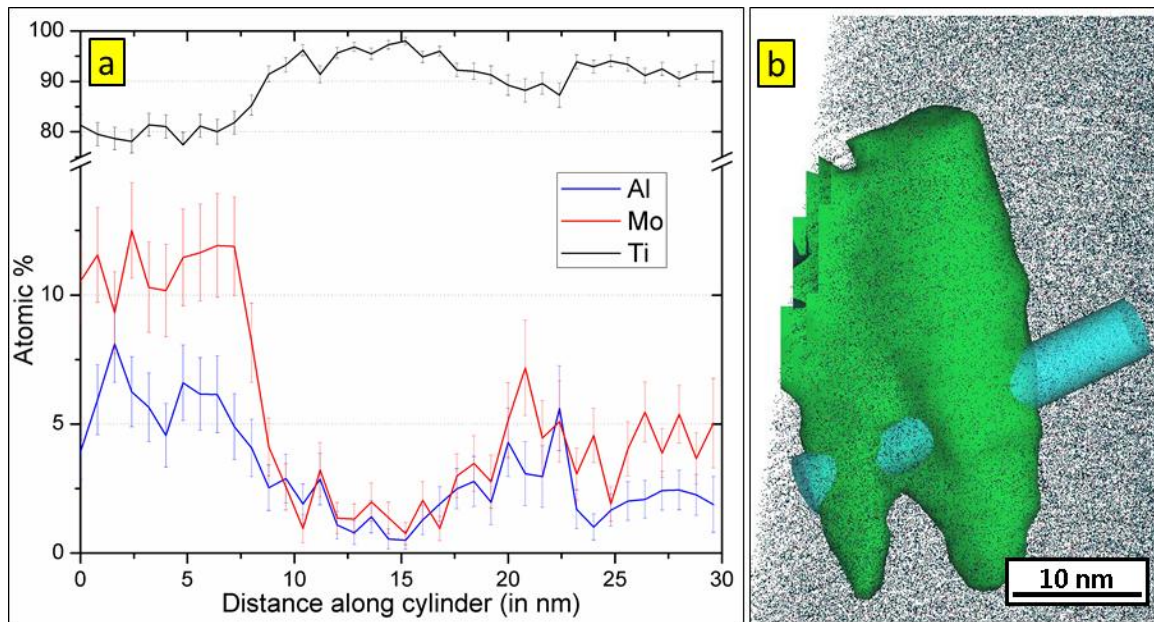
Figure 11: (a) 1D composition profile along cylinder shown in (b). (b) reconstructed tip volume showing omega and alpha precipitate enclosed by iso-concentration surface along with cylinder for 1D comp profile measurement

Based on the results obtained using TEM and 3DAP, the increase in nucleation density and size of omega precipitates upon aging at 350°C was clearly identifiable. However, the overall change in volume fraction of omega phase with time and the consequent changes in beta phase are not clear from the existing experiments. High resolution x-ray diffraction experiments using synchrotron based radiations, with in-situ heating/cooling setup was used to study the phase transformations upon isothermal annealing at 350°C. A Gleeble setup enabled heat treatments to be carried out at high heating/cooling rates with very accurate temperature sensitivity. The specimens used were solutionized above the beta transus temperature and water quenched to room temperature prior to the experiments. The starting microstructure thereby contained a small volume fraction of athermal omega precipitates inside the beta matrix. The test involved rapid heating of the samples to 350°C and an isothermal hold for 5 hours. After that, the samples were rapidly heated up to 600°C and held for 1 hour. The samples were eventually fast cooled from 600°C to room temperature. X-Ray diffraction measurements were recorded both during heat up as well as

during the isothermal aging process. A comparison of diffraction patterns obtained at different times is shown in Figure 12 and Figure 13. Intensity versus 2Theta plots for samples at the beginning, at room temperature, along with those obtained at 350°C after aging for 30 minutes, 2.5 hours and 5 hours are shown in Figure 12. The initial pattern at room temperature, shown at the bottom contained intensity peaks for beta phase and athermal omega precipitates, as marked. The angular range contains four peaks for beta phase, β[220], β[310], β[222], β[312]. Peaks for omega phase, [220]ω and [311]ω are seen to increase in intensity with increasing aging time at 350°C. A slight leftward shift of almost same magnitude for all peaks on heating from room temperature to 350°C is seen due to lattice thermal expansion. Figure 13 shows continuation of the comparison with in-situ diffraction measurements obtained after 30min/60min aging at 600°C and that obtained after cooling to room temperature. The intensity peaks for omega phase could be seen to disappear as the sample reaches 600°C. Intensity peaks for alpha precipitates start to appear upon aging at 600°C. The peaks for beta phase are seen to shift rightwards, in contradiction to the expected leftwards shift due to lattice thermal expansion going from 350°C to 600°C. This is marked in the figure with a dotted line along the β[310] peak. The shift could be attributed to the dominating effect of compositional partitioning occurring at 600°C due to alpha precipitation. The beta phase gets richer in Mo with increasing precipitation of alpha phase. Mo, due to its smaller atomic radius compared to Ti, decreases the lattice parameter of beta phase and shifts the beta peaks to higher 2theta angles.
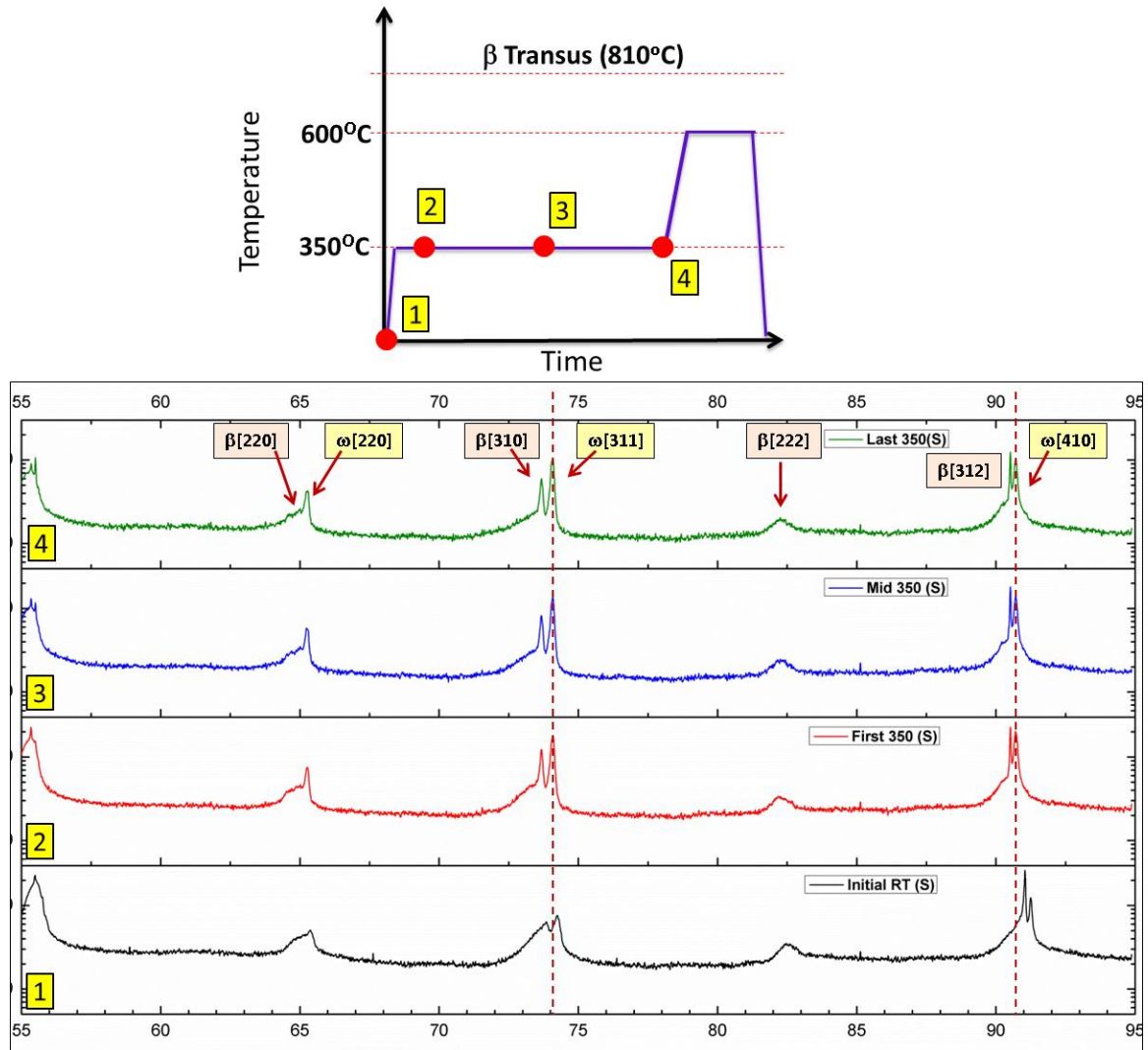
Figure 12: (Top) Heating cycle schematic depicting specific points at which x-ray scans were performed, (Bottom) Intensity versus 2Theta plots measured in-situ during heat treatment for (1) bsol+WQ sample, (2), (3), (4) after aging at 350°C for 30mins, 2.5hrs, and 5hrs respectively. The points are also marked on the above shown schematic.
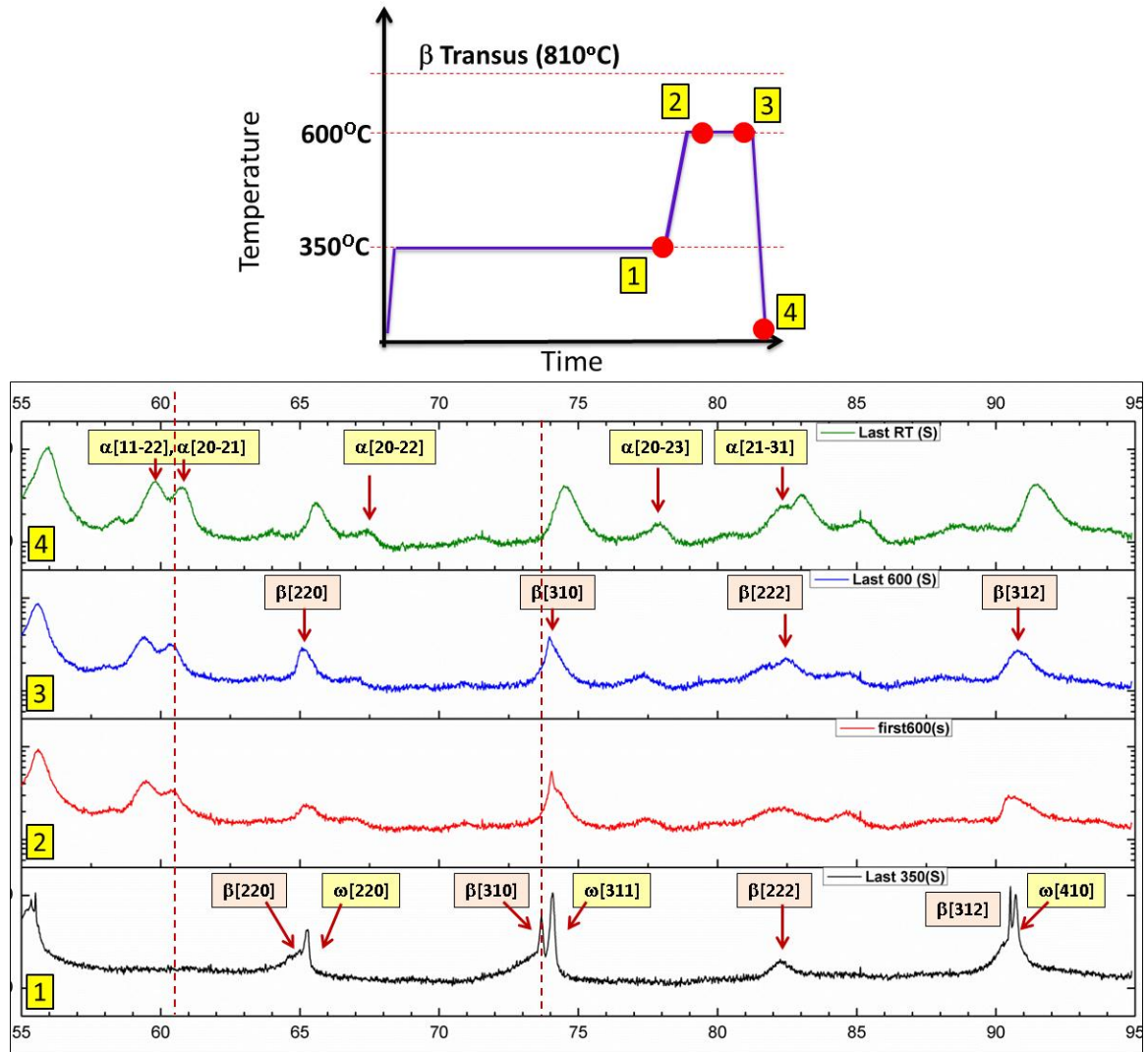
Figure 13: (Top) Heating cycle schematic showing specific points at which x-ray scans were performed, (Bottom) Intensity versus 2Theta plots measured in-situ during heat treatment at different stages; (1) 350°C for 5hrs, (2) 350°C/5hr + 600°C/30min (3) 350°C/5hr + 600°C/1hr (4) 350°C/5hr + 600°C/1hr + WQ to room temperature. The points are also marked on the schematic shown above.

The practical importance of omega precipitates is due to their potential of acting as heterogeneous nucleation sites for subsequent alpha precipitation. Thereby, in order to understand the effect of omega precipitation on alpha nucleation/growth, samples after different stages of aging at 350°C were taken out and aged at 600°C for 1 hour. SEM micrographs obtained show fine sized alpha precipitation throughout the beta matrix after 600°C heat treatment for all cases of prior 350°C aging. Figure 14 shows SEM micrographs from samples with 0, 5, 20 and 100 hour aging time at 350°C prior to 600°C aging. For case

of 0 hr aging at 350°C, in which sample was directly heated to 600°C from water quenched condition, there is very less intragranular precipitation but more grain boundary allotriomorphs observed. The size of precipitates in Figure 14(b) can be seen to be coarser than those for Figure 14(c) and (d). Increasing precipitation of omega phase at 350°C leads to more nucleation sites for alpha precipitation, resulting in finer sized α precipitates. These results clearly suggest that omega precipitates and its nucleation density play a significant role in alpha precipitation and the resulting size scale of alpha precipitates.
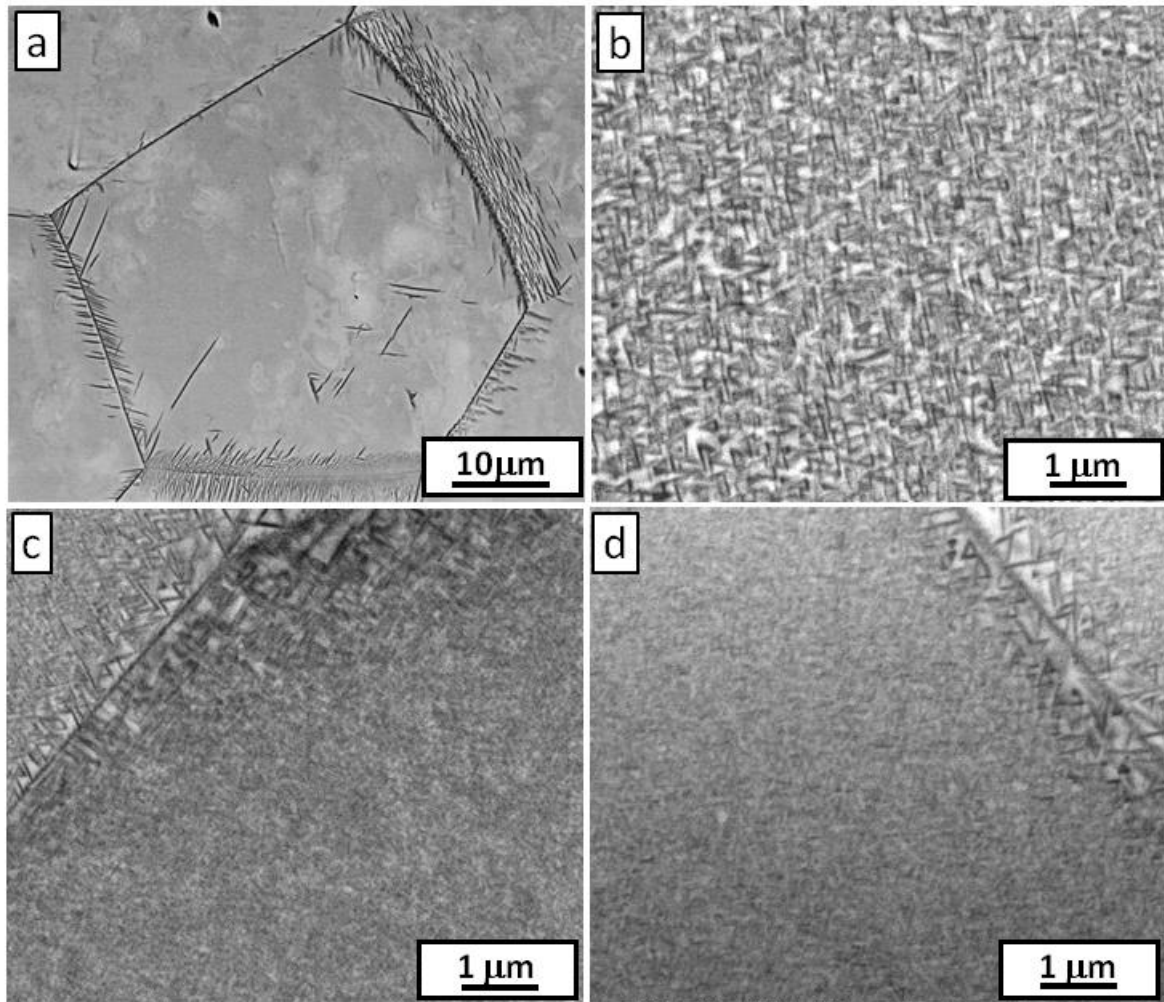
Figure 14: SEM micrographs obtained using BSE mode for samples aged at (a) 600°C/1hr (b) 350°C/5hr + 600°C/1hr (c) 350°C/20hr + 600°C/1hr (d) 350°C/100hr + 600°C/1hr.
Note: (a) is of a different magnification than (b), (c), and (d)

Analysis of omega precipitation using TEM and synchrotron based x-ray diffraction studies shows increase in the nucleation density, size scale and overall volume fraction of it upon isothermal aging at 350°C. The omega precipitates are noted to be mainly titanium rich pockets with all other alloying additions being rejected from them. Two step aging treatment and subsequent SEM analysis helped us identify the effect of omega precipitation on alpha nucleation and size scale of alpha precipitates.

3.4.3. Microstructure Evolution upon Isothermal Aging Above ω Solvus Temperature

On annealing the alloy at temperature above the omega solvus temperature, the dissolution of the athermal omega precipitates occurs. In order to study the sequence of phase transformations that occur on annealing above omega solvus temperature, the alloy was isothermally heat treated at 400°C for various intervals of time. Selected area diffraction patterns collected along <113>β zone axis after different stages of isothermal annealing have been shown in Figure 15. Intensity peaks for omega phase are seen at 1/3 and 2/3 {112} positions in the starting material, corresponding to athermal omega precipitates. The intensity of these omega peaks is seen to decrease after aging for 2 hours at 400°C. This indicates the dissolution of omega precipitates present in the starting material upon aging at 400°C, which confirms the assumption that 400°C is above the omega solvus temperature. On further aging till 5hrs, intensity maxima's for alpha phase are seen halfway along the {112}β direction shown in Figure 15(c). Intensity spots for alpha phase are seen to be intensifying significantly after 50hrs aging, suggesting large volume fraction of alpha precipitates at this condition. The additional intensity spots are formed due to double diffraction effects. SAD pattern after 5hrs aging shows faint spots for alpha phase, which indicates early stages of nucleation/growth of alpha phase.
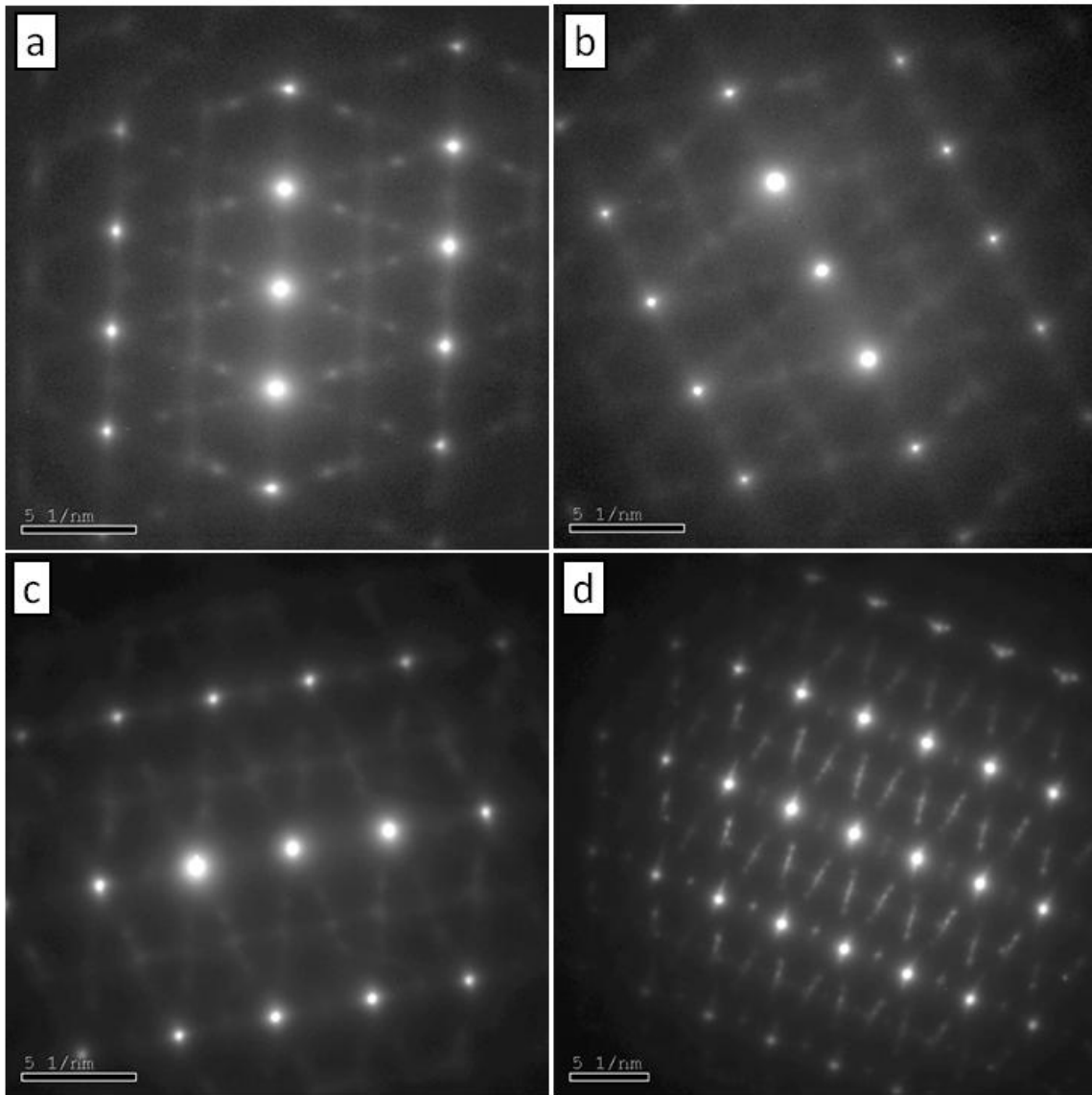
Figure 15: TEM-SAD pattern obtained along [113]β zone axis for (a) bsol + WQ sample (b) sample aged at 400°C/2hr, (c) sample aged at 400°C/5hr, (d) sample aged at 400°C/50hrs

In order to understand the early stages of alpha phase precipitation and determine the possible mechanism of their formation, further analyses was carried out on samples aged for 5 and 50 hours. Early stages of alpha precipitation were observed after aging for 5 hours at 400°C. These precipitates were formed in form of small clusters distributed discreetly in the beta matrix as shown in Figure 16. These clusters, seen as black patches in the bright field TEM micrograph, shown in Figure 16(a), contain multiple variants of alpha phase as

observed in dark field imaging mode. A dark field TEM micrograph that highlights few selected variants of alpha precipitates is shown in Figure 16(b). A higher magnification image of these alpha precipitates, shown in Figure 16(c), shows these precipitates in form of very fine laths with thickness less than 10 nanometers.
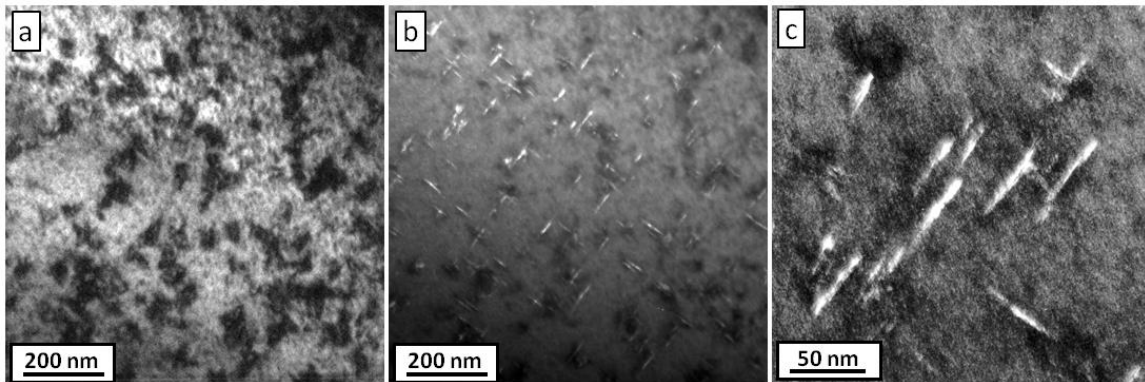
Figure 16: (a) Bright field-TEM micrograph showing clusters of alpha precipitates formed after aging at 400°C for 5hrs (b) Dark field images showing selected variants in these clusters (c) higher magnification image showing extremely fine alpha laths at this aging condition

The morphology and density of these alpha precipitates after aging at 400°C for 5 and 50 hrs was studied using scanning transmission electron microscopy (STEM). STEM micrographs are shown in Figure 17(a) and (b) for 5 and 50hrs aging respectively. The volume fraction and density of alpha precipitates are seen to have increased significantly on prolonged aging at 400°C. However, thickness of the laths doesn't seem to have increased significantly. A triangular self accommodating arrangement of alpha laths [17] generally seen for cases of high precipitate nucleation density, is observed for alpha laths after 50hrs aging. Such clustering of selected variants of α laths has been previously noted in case of α/β titanium alloy, Ti-550[23] as well as for martensitic α plates in pure Ti[24].
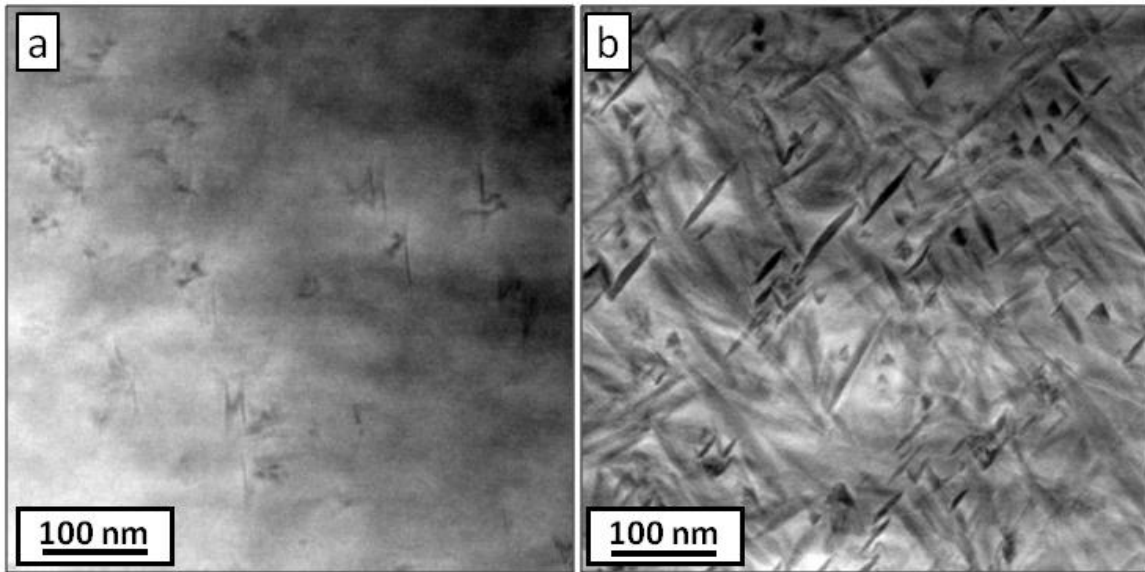
Figure 17: Scanning transmission electron micrographs (STEM) for samples aged at 400°C for (a) 5hrs (b) 50hrs

TEM studies showed the structural evolution of alpha precipitates on aging above the omega solvus temperature. In order to better understand the possible mechanism behind alpha precipitation at 400°C, the compositional evolution of these precipitates from 5hrs to 50hrs was analyzed. APT studies were carried out on samples aged for 5 and 50 hours at 400°C. Figure 18(b) shows an ion map of a clipped section from one of the reconstructed volumes prepared from 5 hours aged samples. Thin lath shaped titanium rich regions were identified in these sections assumably corresponding to alpha precipitates. These regions are found to be enriched in titanium and depleted in molybdenum compared to beta matrix. However, no significant difference in aluminum concentration was observed. The composition of these precipitates is shown with help of a 1-D concentration profile measured along a cylinder going through these alpha laths, as shown in Figure 18(b). Figure 18(a) shows the composition profile with the alpha lath near to the end. The results hint towards nucleation of alpha phase with a non-equilibrium composition when aged at 400°C. Assuming classical nucleation/growth mechanism to be operative at this temperature, the alpha precipitates

would be expected to have much lesser molybdenum concentration than measured using APT experiments.
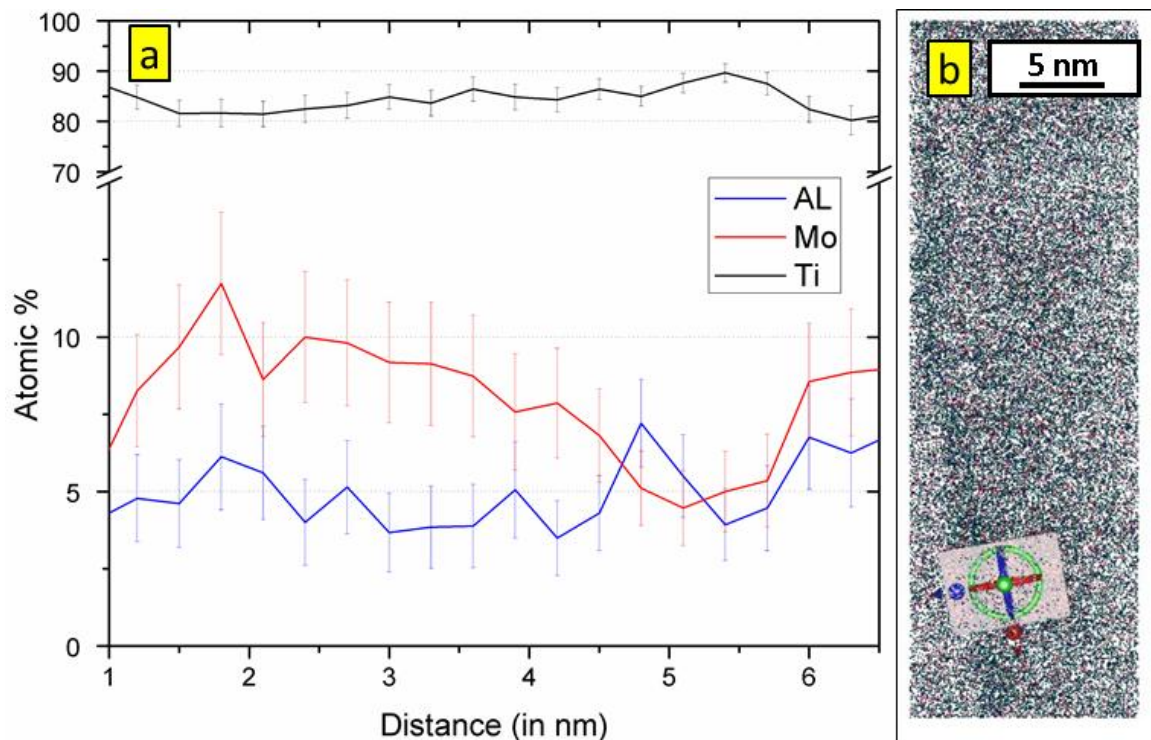
Figure 18: APT analysis of samples aged at 400°C for 5hrs. (a) 1D composition profile along cylinder shown, (b) clipped reconstructed tip volume showing higher Ti ion concentration along a fine alpha lath

Similar analyses were also done for tip reconstructions obtained from 50hrs aged sample, shown in Figure 19, Figure 20. A clipped section of a single tip reconstruction showing titanium (black dots) and Molybdenum (red dots) ions is shown in Figure 19(b). Alpha precipitates enriched in titanium and depleted in molybdenum are seen in form of multiple laths in the section. A 1D composition profile along the shown cylinder was plotted as shown in Figure 19(a). The composition at the center of the cylinder corresponding to alpha precipitates is seen to be enriched in titanium and depleted in molybdenum. The partitioning of elements seems to have increased compared to that after 5hrs aging. The Mo concentration in alpha phase decreased to 3 at% after 50hrs aging. Figure 20(b) shows another instance of an ion map for tip reconstruction from 50hrs aged samples. Multiple fine

36

scale alpha laths can be seen in the clipped reconstruction in form of titanium rich and molybdenum depleted regions. Proximity histogram showing averaged compositional variation across all the captured alpha/beta interfaces is plotted in Figure 20(a). The preference of Mo to partition towards beta phase is clearly observed. Interestingly, Aluminum shows no preference to partition to either alpha or beta phase. This would indicate that there is no thermodynamic driving force for aluminum to partition at 400°C, even though it's well known to be an alpha phase stabilizer. The triangular arrangement of laths seen for high alpha nucleation density is seen in a top view of the reconstructed volume, as shown in Figure 20(c). The triangular arrangement of laths was also observed using TEM studies.
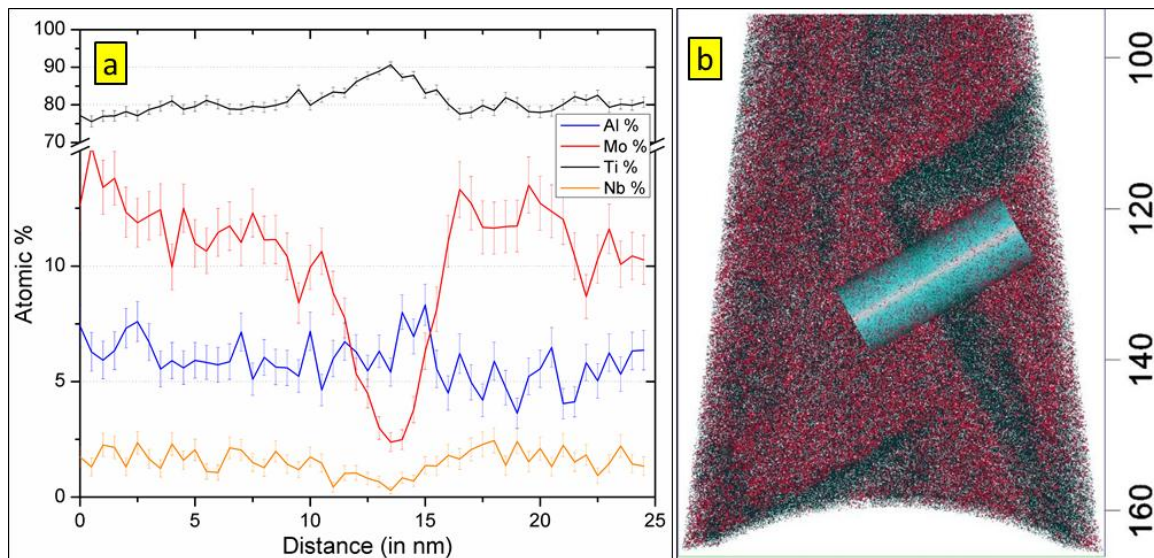
Figure 19: APT analysis of samples aged at 400°C for 50 hrs. (a) 1D composition profile along the cylinder shown, (b) clipped reconstructed tip volume showing Ti (black dots) rich alpha laths in the beta matrix rich in Mo (red dots)
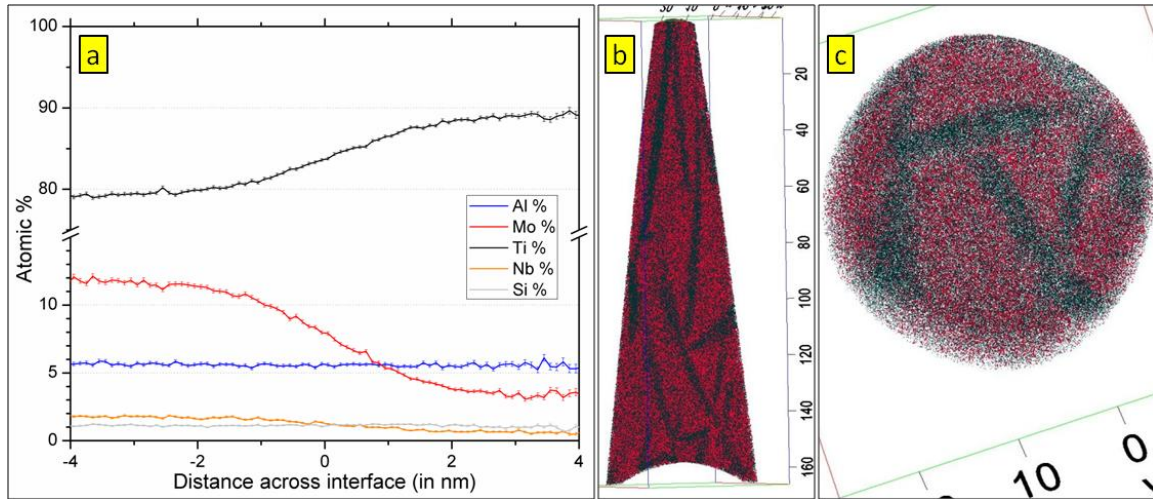
Figure 20: APT analysis of samples aged at 400°C for 50 hrs. (a) Proximity histogram showing averaged compositional changes across all the α/β interface shown, (b) clipped reconstructed tip volume showing alpha laths rich in Ti (black dots) while beta is rich in Mo (red dots), (c) top view of clipped reconstruction showing triangular morphology of alpha precipitates

Dissolution of omega precipitates and subsequent precipitation of alpha phase were also studied using high energy synchrotron based x-ray diffraction experiments. The starting material containing beta phase and athermal omega precipitates was rapidly heated to 400°C and isothermally held for 5 hours. Subsequently, it was reheated to 600°C and isothermally held for 1 hour before being finally fast cooled to room temperature. Diffraction measurements were taken in-situ during heating and after different stages of isothermal annealing at 400°C and 600°C. Figure 21 shows comparison of intensity versus 2Theta plots obtained from samples at the start (at room temperature) along with those obtained at 400°C after aging for 1 hour, 2.5 hours and 5 hours. The initial pattern at room temperature, shown at the bottom contained intensity peaks for beta phase and athermal omega precipitates, as marked. The angular range contains three peaks for beta phase, β[110], β[200], β[211]. Peak intensity for omega phase, [200]ω is seen to decrease with increasing aging time at 400°C. Intensity peaks for alpha phase, α[10-11] and α[10-12], could be identified after aging at 400°C for 2 hours, as seen in the last two diffraction patterns.

Figure 22 shows continuation of the above comparison with in-situ diffraction measurements obtained after 30min/60min aging at 600°C and that obtained after cooling to room temperature. The intensity peaks for alpha phase could be seen to grow significantly upon 600°C aging. A significant leftwards shift in the case of all alpha peaks is observed upon heating to 600°C. The magnitude of the shift is considerably more than the shift observed upon cooling samples from 600°C to room temperature. Thus, the shift going from 400°C to 600°C could not only be due to lattice thermal expansion. The additional effect of change in composition of alpha precipitate affects the peak shift. Upon heating to 600°C, there is much more significant partitioning of alloying elements, especially molybdenum, between alpha and beta phases. Lesser content of Mo in alpha at 600°C, increases its lattice parameter relatively owing to the small atomic size of molybdenum. Increase in lattice parameter results in shifting of peaks towards lower 2theta angles. The peaks for beta phase are seen to shift rightwards, in contradiction to the expected leftwards shift due to lattice expansion going from 400°C to 600°C. This is marked in the figure with a dotted line along the β[200] peak. The shift could be attributed to the dominating effect of compositional partitioning occurring at 600°C due to alpha precipitation. The beta phase gets richer in Mo with increasing precipitation of alpha phase. Mo, due to its smaller atomic radius compared to Ti, decreases the lattice parameter of beta phase and shifts the beta peaks to higher 2theta angles.
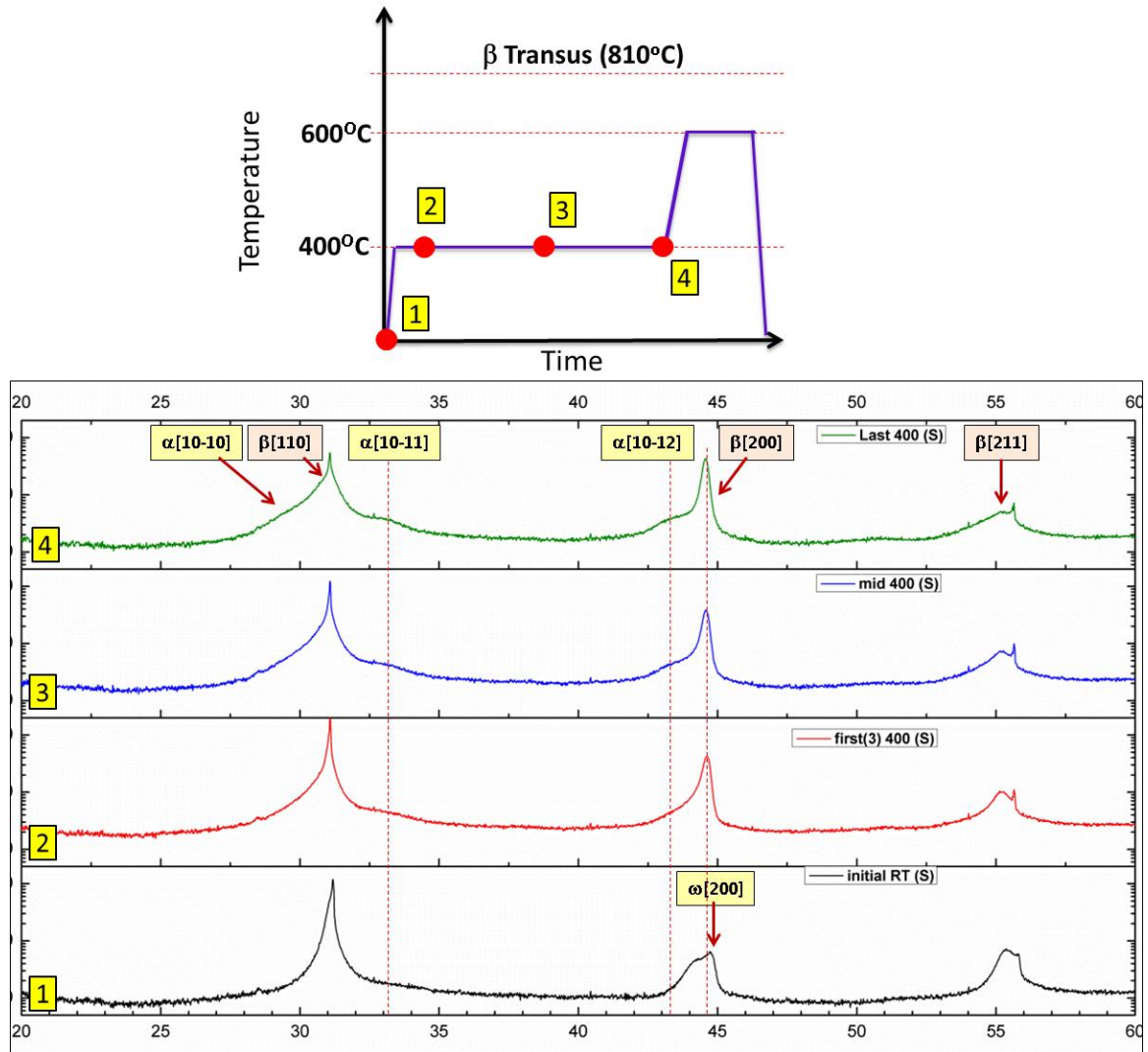
Figure 21: (Top) Heating cycle schematic showing specific points at which x-ray scans were performed, (Bottom) Intensity versus 2Theta plots measured in-situ during heat treatment for (1) bsol+WQ sample, (2), (3), (4) after aging at 400°C for 1hr, 2.5hrs, and 5hrs respectively. The points are also marked on the above shown schematic.
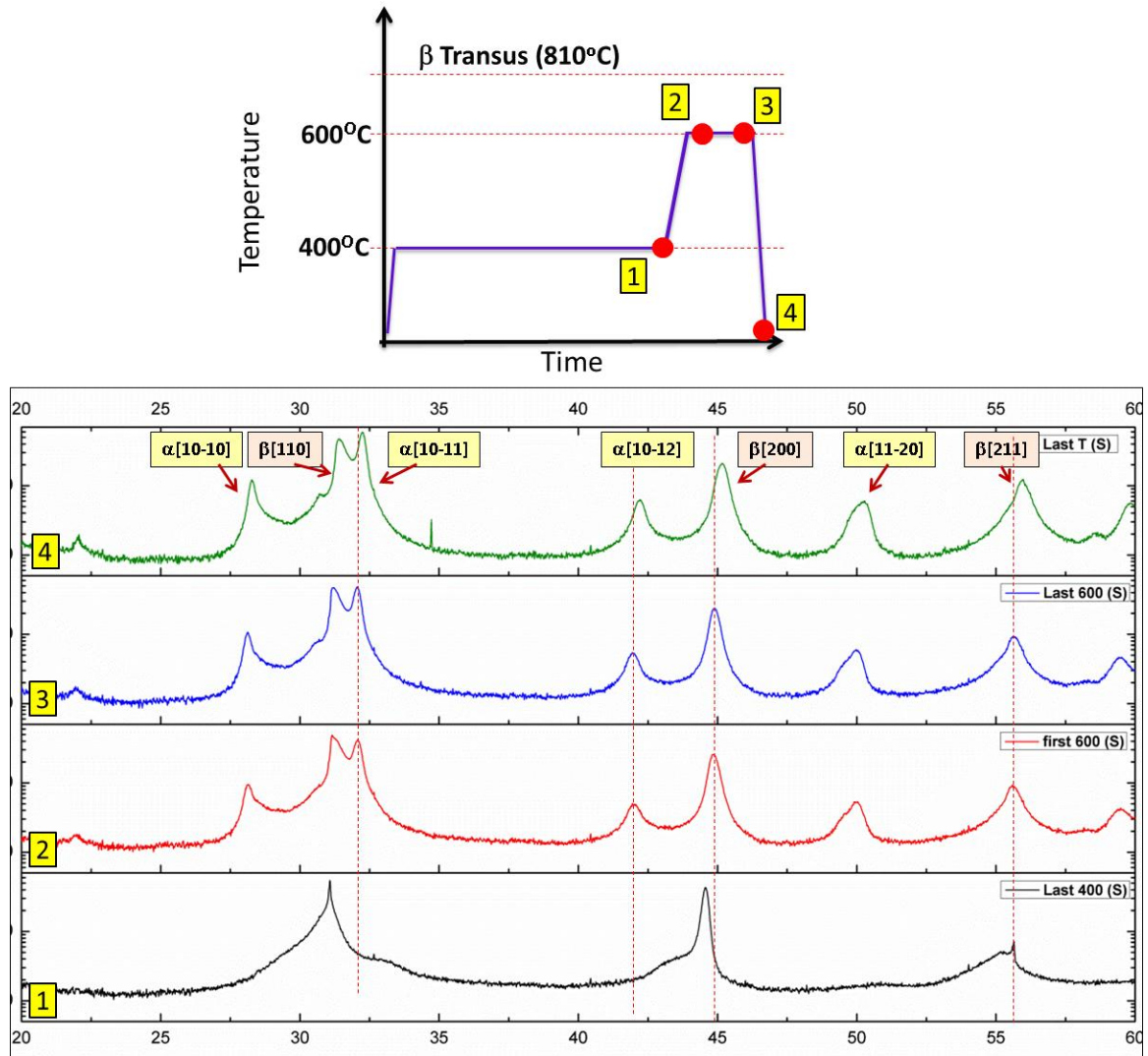
Figure 22: (Top) Heating cycle schematic showing specific points at which x-ray scans were performed, (Bottom) Intensity versus 2Theta plots measured in-situ during heat treatment at different stages; (1) 400°C for 5hrs, (2) 400°C/5hr + 600°C/30min (3) 400°C/5hr + 600°C/1hr (4) 400°C/5hr + 600°C/1hr + WQ to room temperature. The points are also marked on the above shown schematic.

3.5.　　　Summary and Conclusions

The study aimed at understanding the precipitation of omega phase upon isothermal aging below the omega solvus temperature and comprehends its possible influence on subsequent alpha phase precipitation. The precipitation behavior in the absence of omega phase was also studied with help of isothermal aging treatments above the omega solvus temperature. The key understandings resulting from the above studies are:

1. Isothermal omega precipitation occurs on aging below omega solvus temperature for Beta 21S alloy. These precipitates are essentially titanium rich pockets that reject all other alloying additions (less than 1 at% Mo and Al). The nucleation density and size of these precipitates increase on continued aging. Alpha laths could be seen to form in close proximity of these precipitates upon extended aging with slightly higher Mo ($\sim$ 4at%) and Al ($\sim$2at%) concentrations.

2. The role of isothermal omega precipitates in providing heterogeneous nucleation sites for alpha precipitation was verified. Homogeneous intragranular precipitation of fine scale alpha phase was observed for all cases having prior isothermal omega precipitation. The increasing density of omega precipitates could be seen to result in higher density and finer size scale of alpha precipitates upon subsequent high temperature aging.

3. The precipitation sequence above omega solvus (at 400°C) seemed to be dissolution of athermal omega precipitates followed by alpha precipitation. Extremely fine alpha laths are after 5hrs aging is captured using TEM and APT experiments. These laths are seen to nucleate with a composition far from equilibrium values indicating precipitation via a non classical nucleation/growth mechanism.

4. Extremely fine scale alpha laths (thickness less than 10-15 nanometers) are observed after prolonged aging at 400°C. A significant molybdenum partitioning is observed between alpha/beta phases however, there seems to be no driving force for aluminum partitioning.

The alpha laths are seen to be clustered in a triangular arrangement from TEM as well as atom probe analysis. Other beta stabilizing alloying additions such as Nb are also seen to be depleted in the alpha phase.

CHAPTER 4

NON CLASSICAL MECHANISMS FOR HOMOGENEOUS α PRECIPITATION IN

BETA TITANIUM ALLOYS

4.1. Introduction and Motivation

Fine scale homogeneous distribution of alpha precipitates in beta phase matrix is the most favorable microstructure from a high strength application perspective. In most cases the presence of an intermediate metastable phase such as omega precipitates, is seen as the only means to achieve such homogeneous distribution of alpha precipitates. These metastable phases are believed to act as heterogeneous nucleation sites for precipitation of stable alpha phase. The current study aims at identifying and understanding another possible mechanism for homogeneous fine sized alpha precipitation in β-Ti alloys. The precipitation process can be seen clearly to not involve any metastable phases and hence their role can be disregarded.

4.2. Background and Previous Literature

Precipitation strengthening is known to be one of the most significant modes of strengthening in metallic alloys. Fine scale homogeneously distributed second phase in a parent matrix is most desirable microstructure from a properties point of view, especially strength. This has been observed across a number of important alloy systems such as Al based alloys [25], Ni based alloys [26] and also for Ti based alloys. The understanding of these mechanisms to obtain homogeneous precipitation is of significant importance and interest, when modeling the precipitation behavior of these alloys.

In case of titanium alloys, specifically β-Ti alloys, precipitation of HCP alpha phase in matrix of BCC beta matrix is known to improve its mechanical properties. Alpha precipitates are usually seen to precipitate as grain boundary allotriomorphs forming along prior beta grain boundaries, or as widmanstatten plates growing from grain boundary alpha phase or existing widmanstatten plates. In addition to precipitation on heterogeneous nucleation sites, other different mechanisms for alpha precipitation directly from the beta matrix have also been proposed. The first mechanism involves the phase separation of beta phase [27], [28] into two solid solutions, one rich with beta stabilizing elements while the other being lean of it. The solute lean phase is thought to be conducive for the precipitation of alpha phase. The second mechanism necessitates role of the metastable phase, omega phase to act as homogeneously distributed heterogeneous nucleation site for alpha precipitation [17]. The third and more recent mechanism that has been proposed requires no intermediate phase or heterogeneous sites and enables homogeneous alpha precipitation directly in the beta matrix via pseudo spinodal decomposition mechanism [29], [30].

The new mechanism based on pseudo-spinodal decomposition concept states that the transformation is mediated by small compositional fluctuations in the beta matrix when the composition of the alloy is close to the $c_o(T)$ composition for alpha and beta phases. The $c_o(T)$ composition is marked by the intersection of the free energy curves for the two phases. Studies focused on the isothermal annealing of Ti-5553 alloy by Nag et al. [29] highlighted the salient features of the precipitation behavior. A large increase in precipitate density, kinetics of precipitation and homogeneous distribution of second phase was observed with small change in annealing temperature (a change of 50°C). This homogeneous precipitation was shown to occur in absence of beta phase separation or metastable omega precipitates. The precipitate phase has been shown to form with an initial composition far from the

equilibrium precipitate composition and undergoes a continuous change to reach equilibrium values.

The mechanism of the transformation has been described with help of a few schematics as shown in Figure 23. The mechanism involves homogeneous decomposition of the beta phase, with BCC structure, via small compositional fluctuations into solute lean and solute rich phases, which transform into alpha phase with HCP structure. The decomposition mechanism is activated for a given composition, at temperatures where the alloy composition is at close proximity to the $c_o(T)$ composition. In the schematics shown in Figure 23, the alloy composition 'c' is far from the $c_o(T)$ composition at 800^oC. Lowering of temperature causes the free energy curve for BCC phase to move faster compared to HCP phase owing to its higher entropy. This results in the alloy composition getting closer to $c_o(T)$ composition. At close to 600^oC, the alloy composition is sufficiently close to $c_o(T)$ such that small compositional fluctuations in beta matrix would be sufficient to take the beta composition past the $c_o(T)$ point, thereby leading to alpha precipitation. The alpha phase formed due to these fluctuations would initially have a non-equilibrium composition which would move towards the equilibrium value with progress in time. The proposed mechanism [29] was able to explain the changes in precipitation behavior of Ti-5553 alloy and has been established as a viable precipitation mechanism not only in case of beta titanium alloys but also for a large number of transformations involving precipitation of refined distribution of precipitates [30]. Similar studies carried out on another commercial beta titanium alloy; Beta 21S has been discussed in the current work.
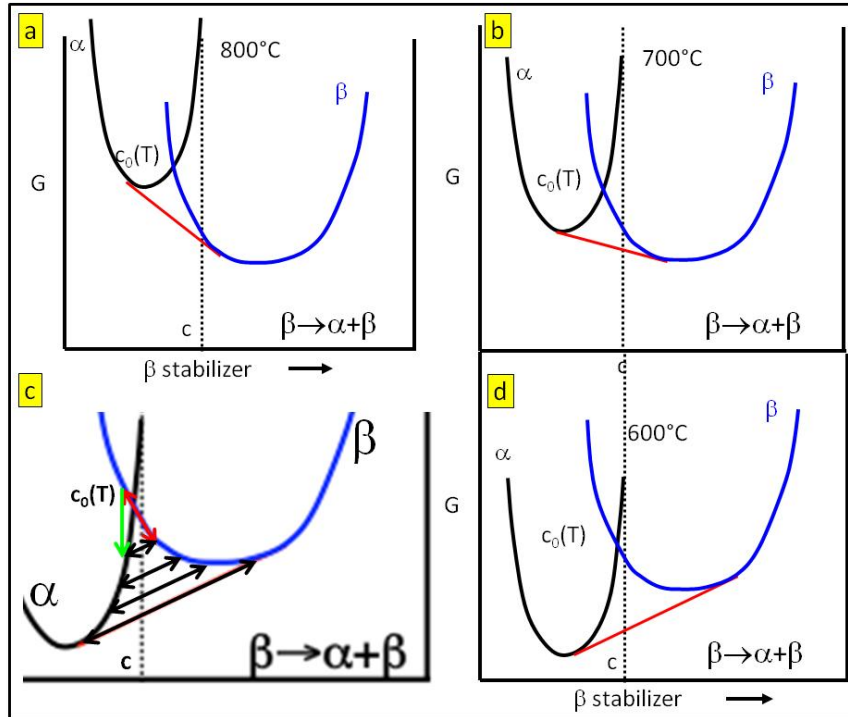
Figure 23: (a-c)Schematics showing free energy versus beta stabilizer plots at different temperatures, (d) schematic showing nucleation of α precipitates with non-equilibrium composition that gradually move towards equilibrium values (pseudo spinodal decomposition mechanism)[29]

4.3. Experimental Procedure

The material used for the current analysis was Beta 21S alloy, obtained in form of cold rolled sheets from TIMET. The heat treatment schedules followed are illustrated by the schematics drawn in Figure 24. The first set of experiments, depicted by Figure 24(a) involved heating the samples above the beta transus temperature, to 900°C and then isothermally holding it for 15 minutes. The samples were subsequently step quenched to different temperatures (650°C, 600°C, 550°C, 500°C) and isothermally aged for various time intervals (1hr-5hrs). The samples were water quenched to room temperature after the isothermal aging treatment. The second set of experiments depicted by Figure 24(b) included heating up and isothermal holding of samples at 900°C for 15 minutes, followed by water quenching to room temperature. The samples were then heated up and isothermally aged at

temperatures, 650°C, 600°C, 550°C, 500°C, for different time intervals followed by water quenching to room temperature.

Specimen preparation for various characterization instruments was done using similar procedure as mentioned earlier. SEM was used to study the variation in nucleation density, size scale and volume fraction of alpha precipitates. Electron back scattered diffraction studies were done to analyze the orientation of alpha precipitates and their relationship with the matrix beta phase. APT experiments were carried out to study the compositional partitioning of the alloying elements at early stages of the transformation (precipitation reaction) and to correlate differences in compositional evolution with the differences observed in precipitation behavior.
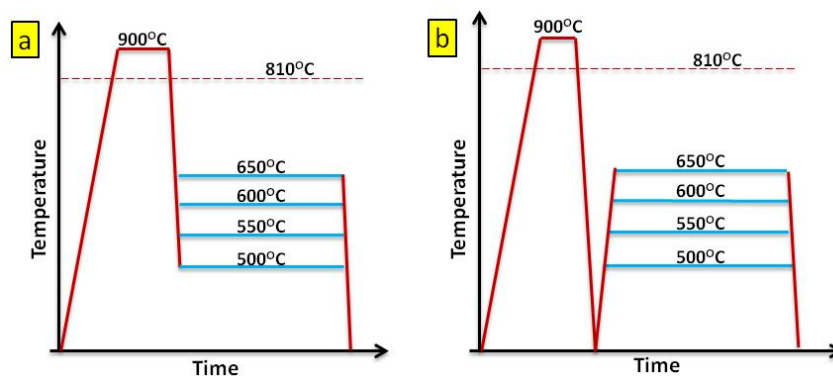
Figure 24: (a) Step quenching heat treatment schedules (b) Beta solutionizing + water quenching to RT followed by direct aging at different temperatures

4.4. Results and Discussion

The current study focused on a commercial β-Ti alloy, Beta 21S, in an effort to possibly identify changes in precipitation behavior as observed for other β-Ti alloys [29]. The analysis showed similar trends in experimental observations during step quenching heating treatments for Beta 21S. Figure 25 shows the microstructure observed using SEM after step quenching from a temperature of 900°C (above the beta transus temperature) and isothermally holding for 1 hour at the different marked temperatures. On comparing the

microstructures for 650°C and 600°C, figure 2(a) and (b) respectively, a decrease in precipitate density is noted. This could be explained considering the 'c' shaped time-temperature transformation (TTT) curve (shown in Figure 25(e)) based on classical nucleation/growth model. Both 650°C and 600°C could be lying below the nose of the TTT curve, and thereby when aged for the same time interval, lesser precipitate density is observed for case of 600°C aging. According to this explanation, isothermal aging at 550°C for the same time interval (1 hour) should have resulted in even lesser precipitate density compared to 600°C condition. On the contrary, a much higher precipitate density and overall volume fraction of α precipitates is observed after aging for 1 hour at 550°C, as shown in Figure 25(c). The observation, similar to those made by Nag et al. for Ti 5553 alloy[29], indicates the possibility of a change in precipitation mechanism when the samples are step quenched below a certain value of undercooling. Higher magnification micrographs for case of 550°C aging, as shown in Figure 25(d), shows a unique self-accommodating triangular arrangement of α laths. The arrangement is likely to help reduce the strain energy associated with such high precipitate density.
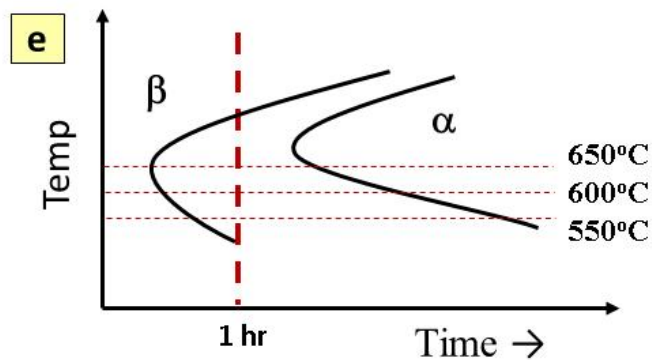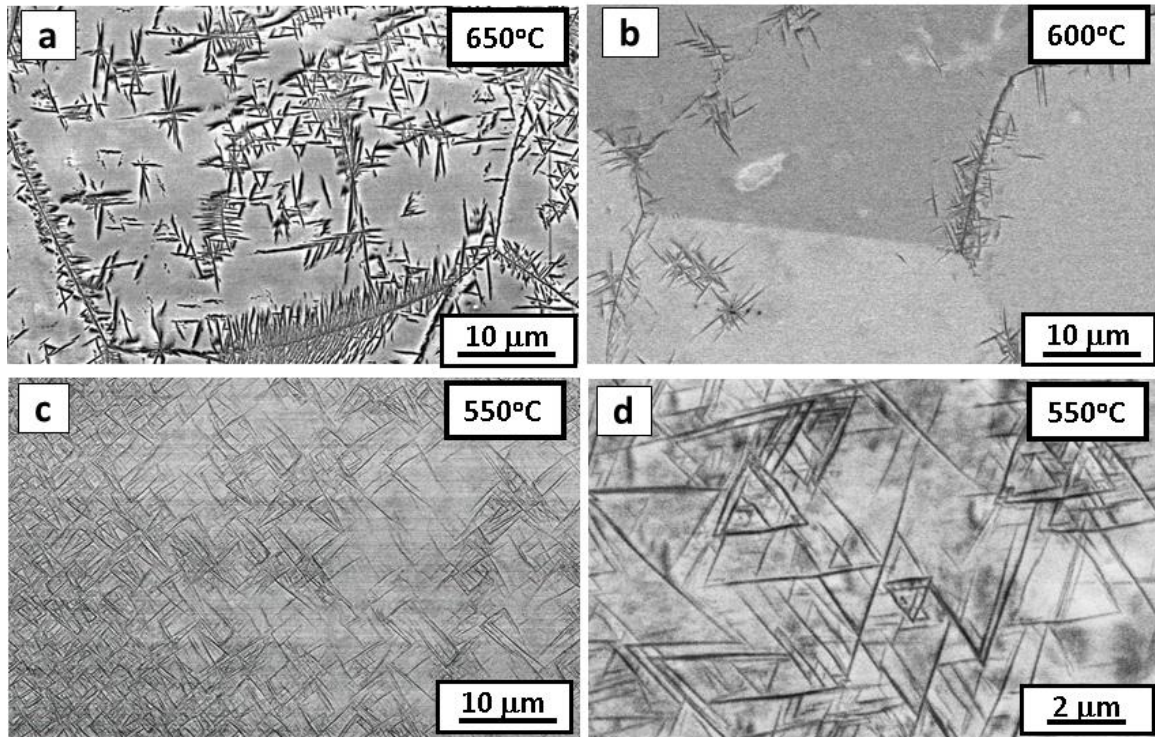
Figure 25: SEM micrographs captured in BSE mode after step quenching heat treatment for 1 hour at (a) 650°C, (b) 600°C, (c) 550°C (d) 550°C-higher magnification (e) possible schematic TTT diagram for Beta 21S

The abrupt change in precipitation behavior upon isothermal annealing at different temperature was also observed when samples were heated up from room temperature. The samples were beta solutionized and water quenched to room temperature prior to the isothermal annealing experiments. Figure 3 shows microstructures obtained using SEM, after isothermally annealing for 1 hour at three different temperatures, as marked in the Figure 26. Similar to the previous case of step quenching, a decrease in precipitate density is observed

going from 650°C to 600°C. However, an abrupt increase in precipitation density occurs when aged at 550°C, shown in Figure 26(c). The observations are difficult to explain with help of classical nucleation/growth mechanism model and hence point towards a change in precipitation mechanism at these temperatures.
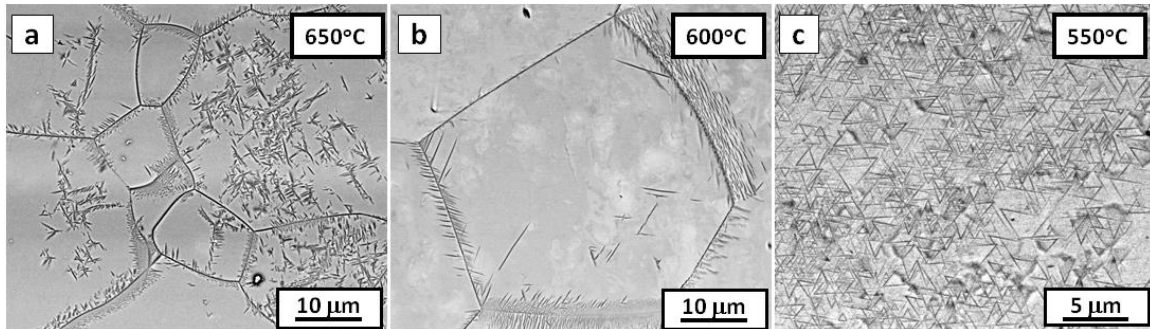
Figure 26: SEM micrographs captured in BSE mode after direct aging treatment for 1 hour at (a) 650°C, (b) 600°C, (c) 550°C

The mechanism of α precipitation via pseudo spinodal decomposition by S. Nag et al. [29] has been suggested as a probable explanation for similar abrupt change in precipitation behavior for Ti-5553 alloy. The important aspects of such a mechanism could be outlined as; (i) requirement of sufficient undercooling for the material composition to lie close to the intersection of the α/β free energy curves, (ii) sufficient kinetics for viable small range compositional fluctuations. The characteristics features of such a precipitation mechanism could be highlighted as (i) α precipitation that occurs homogeneously throughout the matrix (ii) finely sized α precipitates due to large number of nucleation sites (iii) fasters kinetics of α precipitation (iv) non equilibrium composition of α precipitates during early stages of decomposition (v) triangular arrangement of α laths to reduce the strain energy. In order to assess the various features of pseudo-spinodal decomposition in case of Beta 21S, following orientation related studies and composition measurements were carried out.

Electron back scattered diffraction (EBSD) technique was used to study the α/β orientation relationship along with variant selection of α laths during the step quenching experiments. Studies have been carried out on samples that were isothermally aged for longer time intervals at 600°C and 550°C. Longer aging time ensured sufficient growth of α laths to be easily identified and indexed in the EBSD experiments. Figure 3 shows the analysis for samples aged at 600°C for 5 hours. The morphology and arrangement of α precipitates are similar to those observed after aging for 1 hour. An pseudo colored inverse pole figure with alpha and beta precipitates colored according to their orientation, as specified by the color triangle is shown in Figure 27(a). A magnified view of the arrangement of a single cluster of α laths is shown in Figure 27(b). The cluster is found to be comprised of six different variants of α phase, marked by the different colors and numbers. Pole figures for surrounding β phase with {110} and {111} axis and for the shown cluster of α precipitates with {0001} and {11-20} axis have been plotted in Figure 27(c) and (d) respectively. The six different variants of α are seen to exhibit burgers orientation relationship with the surrounding β phase. These variants of α formed a star like arrangement, possibly having a common nucleation point at the center.
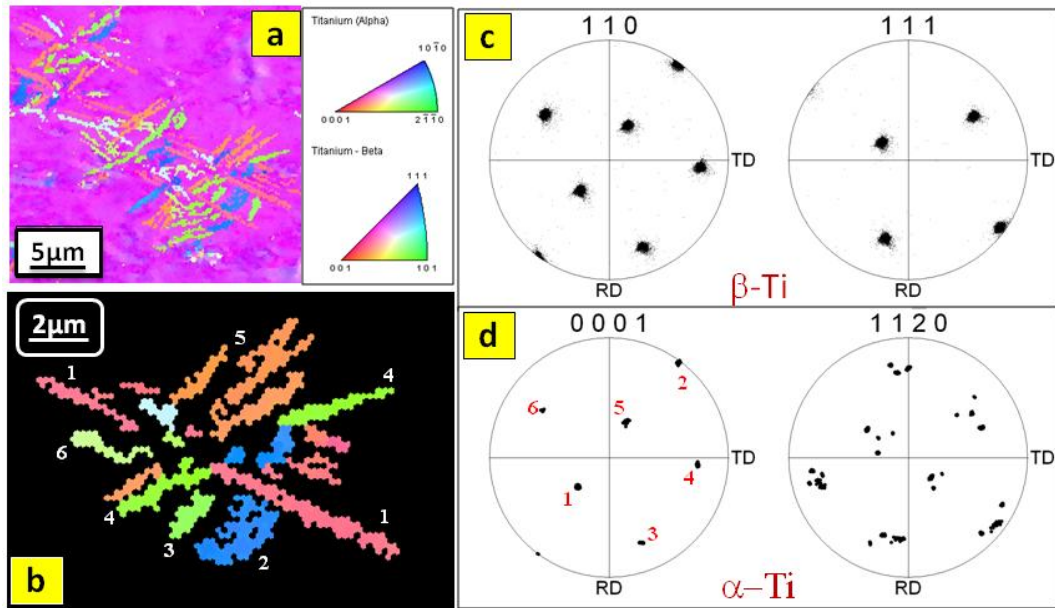
Figure 27: EBSD analysis for samples aged at 600°C for 5 hours, (a) Inverse pole figure(IPF) showing beta and alpha phases (b) clipped IPF of a cluster of alpha precipitates (c) pole figures for beta phase along [110] and [111] axis, (d) pole figure of alpha phase shown in (b) along [0001] and [11-20] axis

In case of aging at 550°C, a different arrangement of α laths is observed. Figure 28 shows the analysis after EBSD studies were carried on these samples. An inverse pole figure for α precipitates, Figure 28(a), shows the homogeneously distributed intragranular precipitates in the β matrix. Multiple variants of α depicted by the different pseudo colors could be seen to have precipitated. A selected cluster of α precipitates is magnified and shown in Figure 28(b). The cluster is made of three different α variants, which are seen to form a unique triangular arrangement. The individual orientation of the laths can be ascertained using the pseudo-color map shown. Pole figures for the shown cluster of α laths along {0001}, {11-20} poles along with that of surrounding β phase along {110}, {111} poles are shown in Figure 28(c) and (d) respectively. The three α variants are seen to share a common {11-20} pole that also aligns with a specific {111} pole of the β matrix. The three variants satisfy the burgers orientation relationship and share the burgers {111} pole common to all of them. This unique clustering of three variants has been reported by other researchers

53

[23], [24] where high nucleation density of precipitates is observed. The triangular clustering of three variants provides the greatest degree of self accommodation, and thereby helps reduce the overall strain energy of the system.
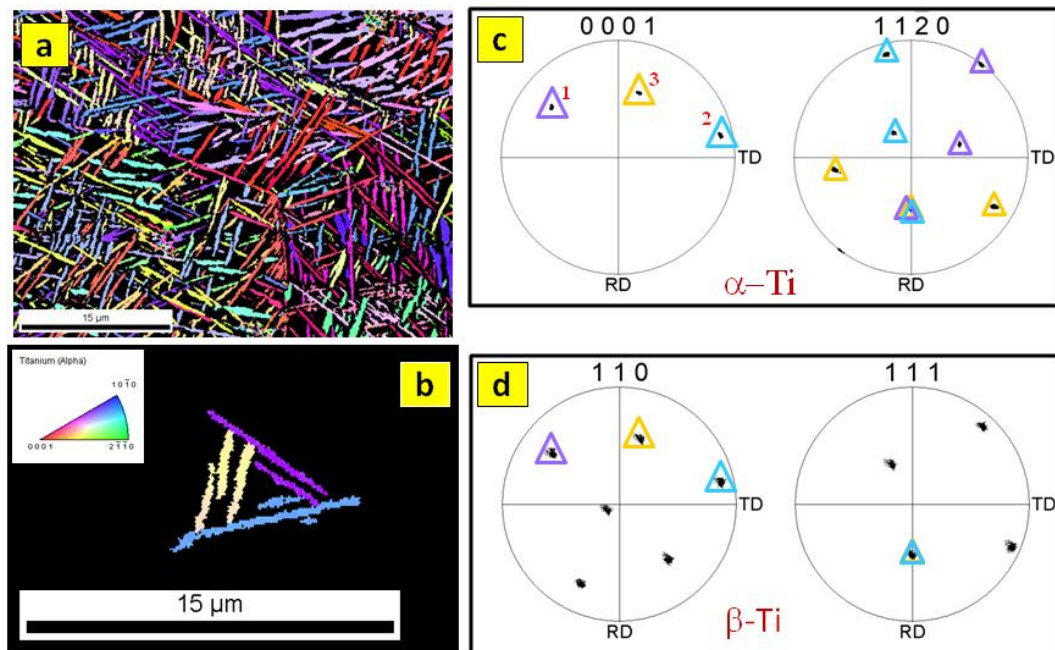
Figure 28:EBSD analysis for samples aged at 550°C for 5 hours, (a) Inverse pole figure (IPF) showing multiple variants of alpha phase, (b) clipped IPF showing one set of triangularly arranged alpha laths, (c) pole figures for alpha phase shown in (b) along [0001] and [11-20] axis, (d) pole figure for beta phase along [110] and [111] axis

Atom probe tomography studies were carried out to capture compositional partitioning between alpha and beta phases, in the early stages of precipitation. Two sets of APT specimens were prepared, one from samples aged at 600°C for 1 hour while the other from samples aged at 550°C for 1 hour. The theory behind pseudospinodal mechanism suggested non equilibrium composition for alpha precipitates in case of 550°C aging, provided 1 hour is still at an early stage of precipitation. Figure 29 shows tip reconstructions obtained after analyzing APT results from samples aged at 550°C. Figure 29(b) shows an ion

map for the reconstruction, with Mo atoms denoted by red dots and Aluminum ions denoted by blue dots. Higher density of Mo in beta phase and Al in alpha phase is clearly observed.
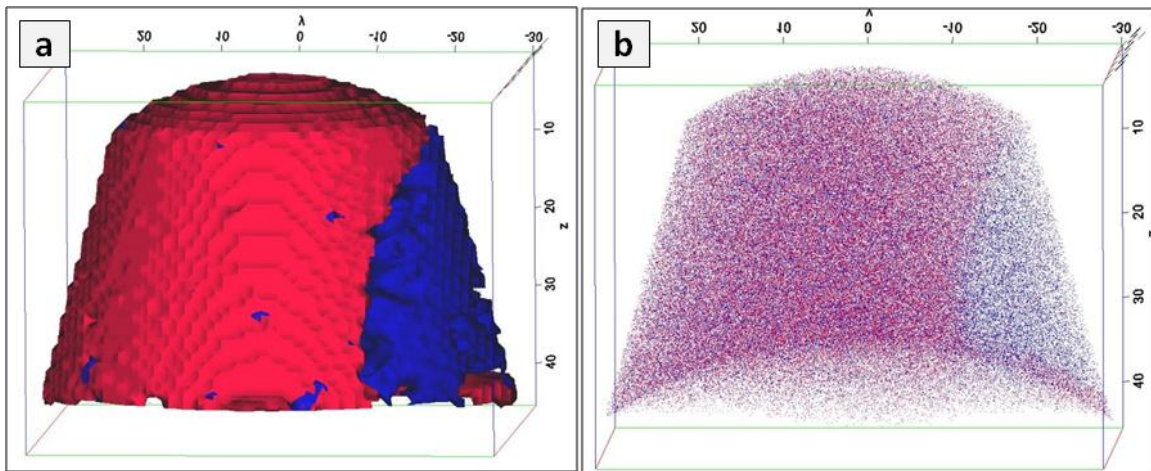
Figure 29: APT analysis for samples aged at 550°C for 1 hour, (a) Filled iso-concentration (Mo - 10at%) surface where beta phase is rich in Mo (red) and alpha phase is rich in Al (blue), (b)Ion map for the reconstructed volume with red dots (Mo) and blue dots (Al)

Figure 30 shows a proximity histogram across the alpha beta interface in case of samples aged at 550°C for 1 hour. A clear partitioning of alloying additions between alpha and beta phases is identified. The alpha phase is seen to have enriched in Al (~8-9at%) and depleted in Mo (~1at%). The composition of beta phase would depend on the extent of transformation (or the amount of alpha formed) and the partitioning of elements. A small amount of oxygen content in the specimen is seen to preferably partition towards alpha phase.

The results from APT studies on samples aged at 600°C for 1 hour are shown in Figure 31. In Figure 31(a), the alpha lath is represented by the Al filled iso-concentration surface (solid blue region) while the Mo filled iso-concentration surface (solid red region) represents the beta phase. An ion map along the top view for the reconstructed volume is also shown in Figure 31(b). The alpha lath region is seen to be rich in Al (blue dots) while beta is rich in Mo (red dots). The sharp flat interface between the two phases is also seen.
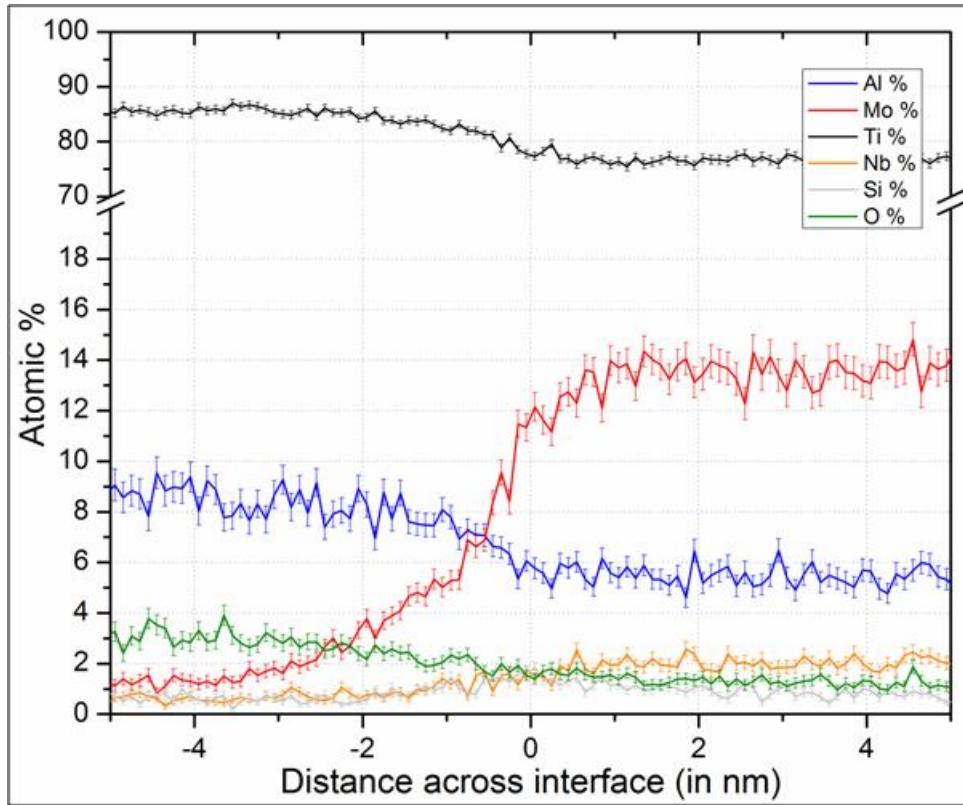
Figure 30: Proximity histogram showing compositional partitioning between alpha and beta phase averaged along the entire interface, for samples aged at 550°C for 1 hour
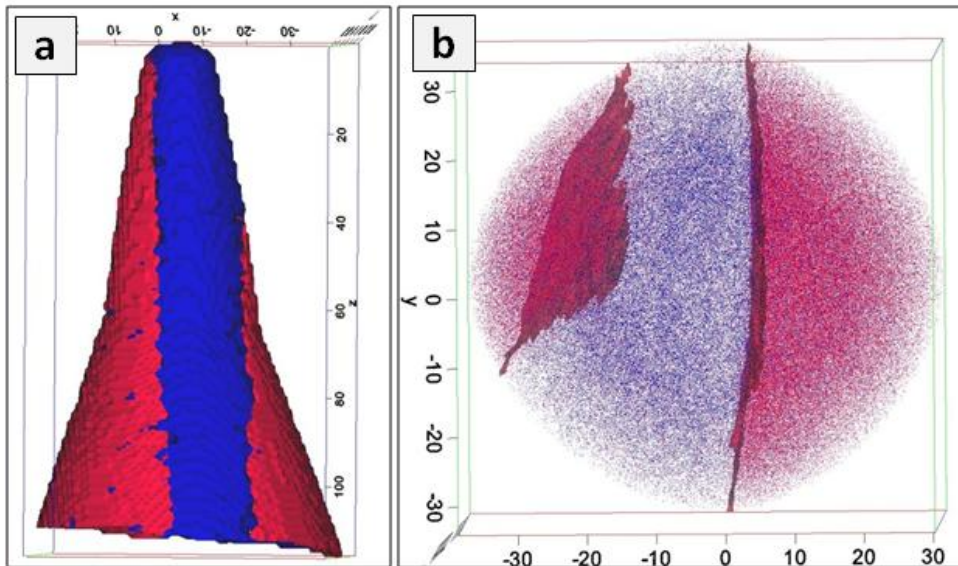
Figure 31: APT analysis for samples aged at 600°C for 1 hour, (a) Filled iso-concentration (Mo - 10at%) surface where beta phase is rich in Mo (red) and alpha phase is rich in Al (blue), (b) Ion map shown along with interfaces for the reconstructed volume with red dots (Mo) and blue dots (Al)

Figure 32 shows a proximity histogram plotted across one of the alpha beta interface shown in Figure 31(b). A clear partitioning of alloying additions is seen between alpha and beta phases. The alpha phase is enriched in Al (~9at%) and depleted in Mo (~1at%). Other beta stabilizers such as Nb also partition towards beta phase. The oxygen content in the specific APT specimens could possibly be influenced by sample preparation and storage conditions. However, preference of oxygen to partition towards alpha phase is observed. This is in accordance with the knowledge of oxygen being an alpha phase stabilizer.
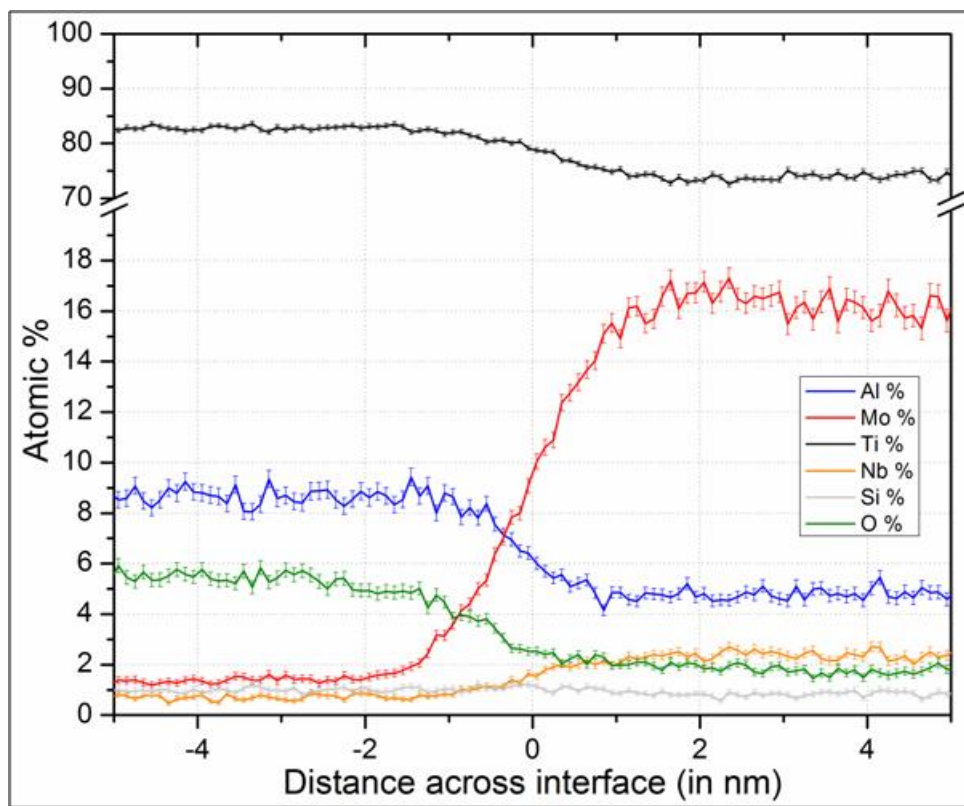
Figure 32: Proximity histogram showing compositional partitioning across alpha beta interface averaged over the entire interface, for samples aged at 600°C for 1 hour

4.5. Conclusion

The current work shows evidence of pseudo-spinodal decomposition occurring in case of a commercial β-Ti alloy, Beta 21S. Similar to earlier observations made for Ti-5553 alloy, an abrupt increase in precipitation density, volume fraction, homogeneous distribution of

precipitates was observed. These observations were made for both step quenching and direct aging heat treatments ruling out the possible role of low temperature metastable phases. A difference in the clustering of alpha laths was seen in cases with high density of alpha precipitates. The laths seemed to form a self-accommodating triangular arrangement comprising of only three crystallographic α variants. In order to achieve the maximum degree of self-accommodation, the three variants in the cluster shared a common {11-20} pole which also aligns with a specific {111} pole of the surrounding β phase. Pseudo-spinodal mechanism suggested α phase to have non equilibrium composition at early stages of precipitation compared to classical nucleation/growth mechanism. However, atom probe studies conducted on samples aged for 1hr duration at both temperatures showed no significant differences in α composition. This could be due to the reason that 1 hour is sufficient time for α to achieve equilibrium composition values. The curvature of individual free energy curves and the point of intersection of the α and β free energy curves would also affect the early stage composition of α precipitates. An intersection point ($c_o(T)$) closer to equilibrium α composition would result in α precipitates nucleating with close to equilibrium composition.

CHAPTER 5

INFLUENCE OF OXYGEN ON FINE SCALE α PRECIPITATION DURING

OXIDATION OF β-TI ALLOY; β-21S

5.1. Introduction

In recent years, there has been an increased interest in the use and further development of several β titanium alloys for high temperature aerospace applications due to improved formability, high strength and toughness [6], [31], [32]. The balance of mechanical properties is expected to be dependent on the volume fraction, size, morphology and distribution of α precipitates within the β matrix [33]. However, these β titanium alloys suffer from poor elevated temperature properties, especially oxidation resistance. In addition to the oxide layer, the mechanism and kinetics of formation of an oxygen-enriched α case layer during the oxidation of these alloys play a critical role in limiting their application temperature. Timetal 21s (also known as Beta 21S [9]) has shown great promise in this respect due to its very good high temperature corrosion and oxidation resistance [34].

5.2. Background and Previous Literature

Studies on this alloy have mostly focused on its mechanical and environmental properties [34], [35], although some work has been done regarding the microstructural evolution when subjected to numerous heat treatments [36]. In the oxidation studies on Beta 21S, the surface oxide layer is noted to consist of TiO_2 and Al_2O_3, with kinetics of oxidation primarily governed by rate of diffusion of oxygen and the chemical reaction to form oxide [37]. During the oxidation process there is a considerable ingress of oxygen, moving inwards from oxide-alloy interface, due to the high affinity of oxygen towards titanium. This results in a marked gradient in the density of α precipitation [38]. The current study complements the

previous research in understanding oxygen influence on the formation of α case layer as well as the precipitation of fine-scale α within the β matrix of this alloy.

5.3. Experimental Procedures

Beta21S is a commercially used metastable β-Ti alloy with the following nominal composition, Ti-15Mo-2.7Nb-3Al-0.3Si (in weight percent). Thin plates of Beta 21S, β-solutionized at 900ºC for 30 minutes followed by water quenching to get a single phase β microstructure, were subjected to open air oxidation heat treatments at temperature of 650°C for duration of 50hrs. Cross sectional specimens prepared from the oxidized plates were investigated in detail using scanning electron microscopy (SEM) and energy dispersive spectroscopy (EDS), carried out in a FEI Sirion™ FEG instrument operating at 15 keV. Specimens for transmission electron microscopy (FEI Tecnai F20™-FEG) were prepared using a dual-beam focused ion beam (FIB), specifically the FEI Nova Nanolab 200™ system. X-ray diffraction studies were conducted in a Rigaku X-Ray Diffractometer. Nanoindentation studies were conducted using a Nanoindenter XP™ system from MTS instrument. Electron probe micro analysis (EPMA) was conducted with a Cameca SX100 at Air Force Research Laboratory (AFRL). Atom probe studies were carried out using a LEAP 3000X^{TM} local electrode atom probe system from Cameca Instruments Inc. All atom probe experiments were carried out in the voltage evaporation mode at a temperature of 60K, with the evaporation rate varying from 0.7 %. Data analysis was performed using IVAS 3.6.6^{TM} software.

5.4. Results and Discussions

Figure 33(a) shows a cross section secondary electron (SE) image of an oxidized Beta 21S sample wherein brighter region on the right denote the oxide layer. A significant variation in the size-scale and nucleation density of the α precipitates with distance from the

oxide-alloy interface is observed. This is more clearly visible in the high magnification backscattered electron (BSE) image shown in Figure 33(c). Thus in the left of this image large scale α laths, representing the bulk microstructure, are present. On moving away from the oxide-alloy interface, the size scale of the α precipitates decreases substantially. Near the oxide layer, the size of these laths is extremely fine ($< 1\mu$m).

Figure 33(b) shows the variation in hardness values, measured by nano-indentation, as a function of distance from the oxide-alloy interface. This curve shows higher hardness values near the oxide layer, where finer α precipitates are present, as opposed to the values obtained far into the bulk of the specimen. Thus a typical hardness reading taken at 5μm from the oxide-alloy interface is ~8.5 GPa while it is only ~5GPa at a distance of 35μm from this interface. The increase in the hardness values could be attributed to the finer size scale of α precipitates and the presence of oxygen in the interstitial sites. Similar results were obtained by previous researchers, where the mechanical property values such as micro hardness and tensile strength of the alloy seemed to vary quite significantly with oxygen content [37], [39]. Figure 33(d) shows a plot for concentration of oxygen near the oxide alloy interface measured using SEM-EDS. It shows the variation in oxygen counts measured from the oxide surface going into the matrix. The graph shows higher amounts of oxygen count in the oxide region and a sharp decline with the curve flattening out at a distance of ~20μm.

Theoretical analysis to study the kinetics of oxygen diffusion into thin sheets of β-21S alloy has been carried out by Sansoz et al. [40]. Samples used for the study were initially duplex aged to result in an $\alpha+\beta$ starting microstructure. The oxidation process at temperatures above 545$^{\text{o}}$C is found to be governed by an enhanced diffusion on oxygen into the alloy. The diffusion coefficient for oxygen into the alloy was calculated to be 0.581 cm^2/s. With help of these calculated values, depth of oxygen penetration on oxidizing at 600$^{\text{o}}$C is plotted for

different times and sheet thicknesses. The results show an oxygen penetration of approximately 100μm upon aging for 100hrs at 600°C and around 30μm upon aging for 10hrs. The starting α+β microstructure could be a possible reason for the higher oxygen penetration compared to results obtained in the current work. The higher solubility of oxygen in α-Ti compared to β-Ti could result in easier pathways for oxygen diffusion into the alloy.
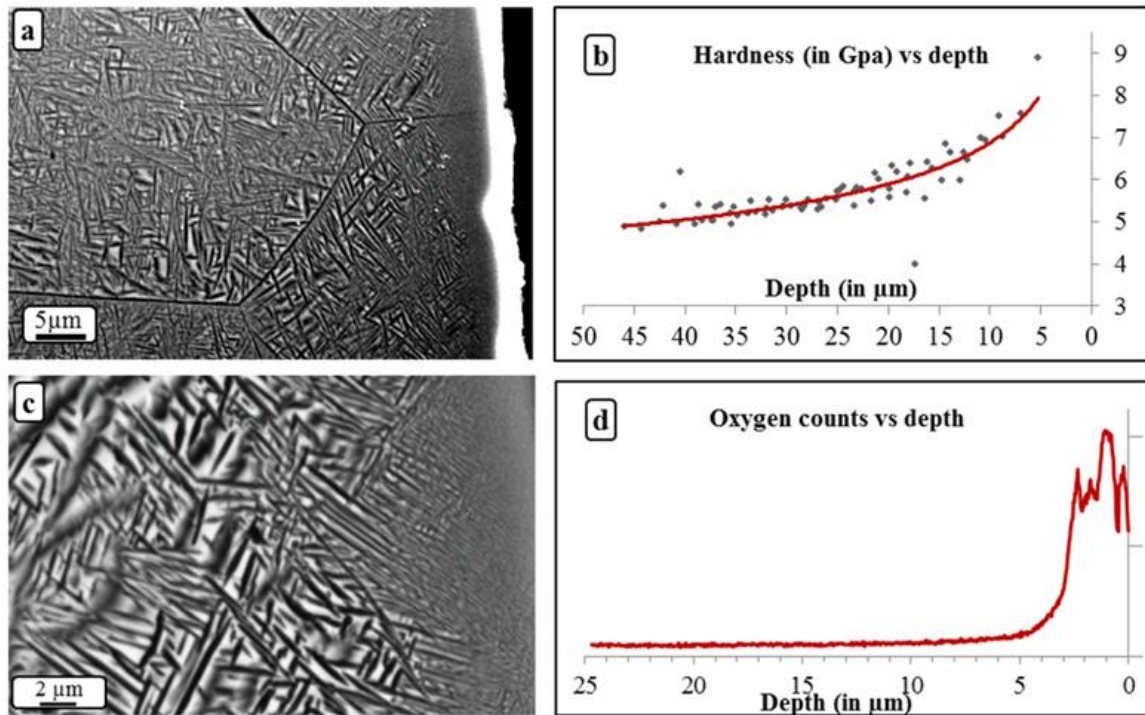
Figure 33: (a) Cross sectional SE image of oxidized Beta 21S showing the oxide layer on the right (b) Hardness values (via nano indentation) versus depth from oxide-alloy interface (c) Higher magnification cross sectional BSE micrograph across the oxide alloy interface, (d) Oxygen concentration profile, measured using SEM-EDS, from oxide to bulk matrix

Electron probe micro-analysis (EPMA) was also used to create a 3D color map, shown in Figure 34(a), depicting oxygen concentration profile across the oxide-alloy interface. It shows sharp oxygen concentration gradient with clear enrichment of oxygen in the fine scale α precipitation zone, up to a depth of ~25μm. The depth of oxygen ingress matches well with the hardness result, which shows an oxygen concentration gradient as far as 30μm from the oxide-alloy interface. From the above observations it is evident that higher

oxygen content corresponds to higher nucleation density of α phase leading to finer α precipitates. This could possibly be explained either due to the effect of oxygen, a α stabilizer, on β transus temperature or its role in providing additional nucleation sites for α precipitation. Figure 34(b) shows similar 3D color map along with its 2D projection for aluminum concentration distribution close to the oxide alloy interface. A clear depletion of aluminum in the oxygen-enriched region is observed from the EPMA concentration maps. The results also show enrichment of aluminum on the oxide surface, providing evidence of alumina formation. This could be further confirmed in subsequent TEM analysis. Reports of alumina at the oxide surface, owing to fast diffusivity of Al compared to other alloying additions and its tendency to form oxide, have been previously documented even for alloys having low Al concentration [37], [38].
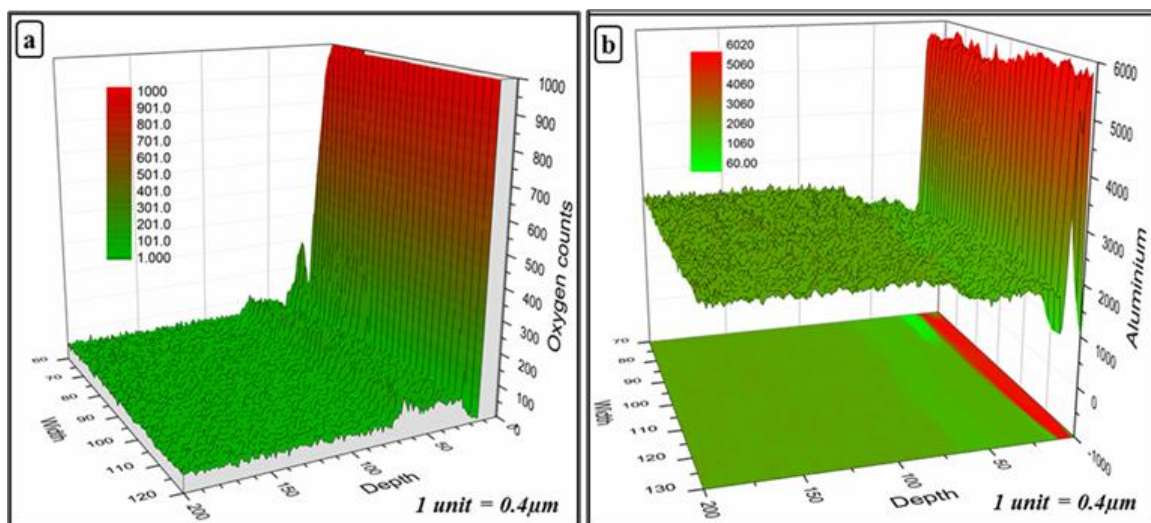
Figure 34: 3D surface plots mapping concentration distributions for (a) Oxygen and (b) Aluminum across the oxide alloy interface using Electron probe micro analyzer.

Figure 35(a) shows a scanning transmission electron microscopy (STEM) image that illustrates the change in microstructure, starting from the oxide layer (marked as 1) on the top to about 10 μm deep into the specimen. The entire oxidized sample based on above microstructure can be roughly divided into distinct layers. Thus the oxide region and the

region of fine scale distribution of seemingly equiaxed α grains have been marked as layer 1 and 2 respectively. These layers are distinctly different from layers 3 and 4 where the α precipitates seem to exhibit more lath-like morphology. The size scale of α laths in layer 3 is quite small (~50-100 nm). However in layer 4 they are ~2-3 μm in length, representing bulk microstructure. A bright field TEM micrograph of layer 1 (Figure 35(b)) shows large number of nanocrystalline oxide grains, with an average grain size of ~20nm. A random orientation of these grains is clearly evident from the rings that are present in the selected area diffraction (SAD) pattern, a quadrant of which is shown as an inset in Figure 35(b). Most of the rings could be indexed consistently based on either rutile (TiO_2) or alumina (Al_2O_3) phases. The rings corresponding to (012) and (113) planes of alumina have been marked by an asterix while the remaining (110), (101) and (211) planes arise from the rutile phase. Similar study conducted on layer 2, consisting of nanoscale equiaxed grains is shown in the bright-field TEM image (Figure 35(c)). From this figure, the average grain size can be estimated to be ~50-100 nm. The figure also shows one such equiaxed α grain (dark grain in the center) to be in strongly diffracting condition. The corresponding SAD pattern shown as an inset in Figure 35(c) can be consistently indexed as <10-10> α. The SAD pattern corresponding to this entire layer (Figure 35(d)) could be consistently indexed as either α-Ti or rutile (TiO_2) phases; the rings correspond to either (11-20) and (10-10) planes of α-Ti or (211), (210) and (101) planes of rutile. Thus the electron diffraction results indicate that this layer consists of a two-phase mixture. However, it is difficult to state with certainty that no β phase was present between the equiaxed α grains. Also, there seems to be a six fold symmetry in the intensity rings corresponding to hexagonal closed packed structure of α-Ti phase. This indicates the presence of a texture within the equiaxed α grains, which could be a subject of further investigation.
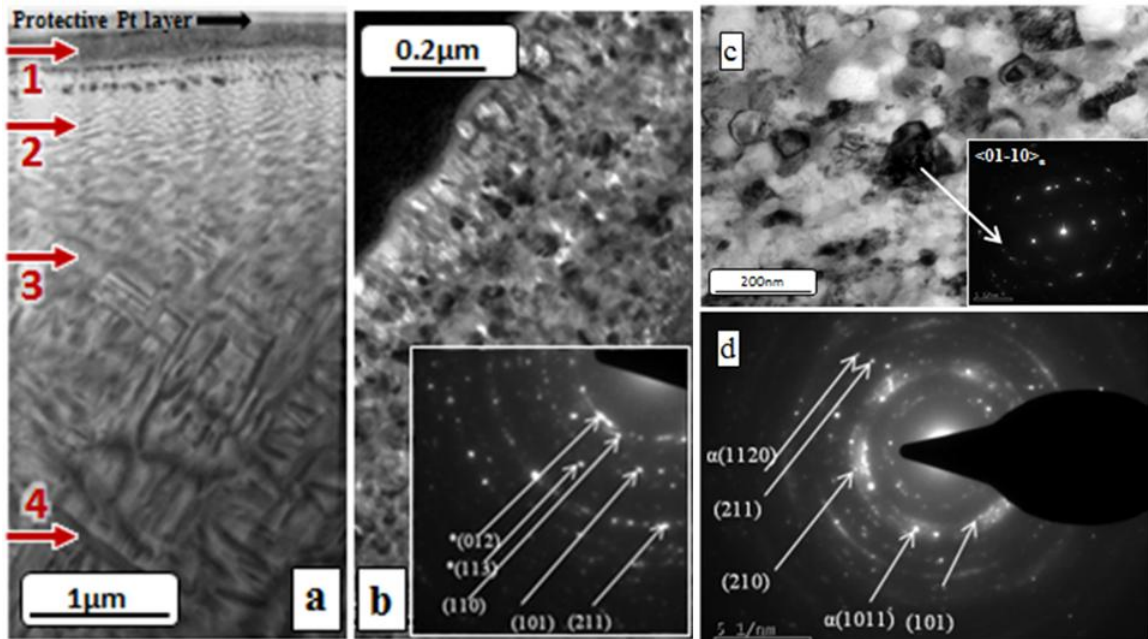
Figure 35: (a) Scanning transmission electron microscopy (STEM) image shows microstructural changes across different layers. (b) Bright field TEM image of the oxide layer (layer 1). Inset shows corresponding selected area diffraction (SAD) pattern. (c) Bright field TEM image of mixed α-Ti and oxide region (layer 2). Inset shows SAD pattern of one equiaxed α grain. (d) SAD pattern from layer 2 with intensity peaks from α-Ti and Rutile.

Figure 36(a) is a bright-field TEM image, showing the microstructural transition from oxide layer (layer 1) to equiaxed morphology of fine scale α grains (layer2) to a more lath-like α morphology (layer 3). Also, a substantial increase in the volume fraction of β is also visible in layer 3. Thus, from left to right in this figure, an increase in α size scale and β volume fraction, and decrease in α nucleation density is clearly visible. The microstructural differences observed among the different layers in Figure 36 are quite apparent and since prior to oxidation the microstructure of this alloy consisted of a compositionally uniform single β phase, they can be attributed to the presence of an oxygen concentration gradient. The figure also contains a sequence of selected area diffraction patterns obtained at various depths from the oxide-alloy interface. A gradient in oxide intensity is observed along with an increasing six fold symmetry for α precipitates. The diffraction patterns also suggest the existence of a two phase region comprising of α-Ti and oxide (rutile).
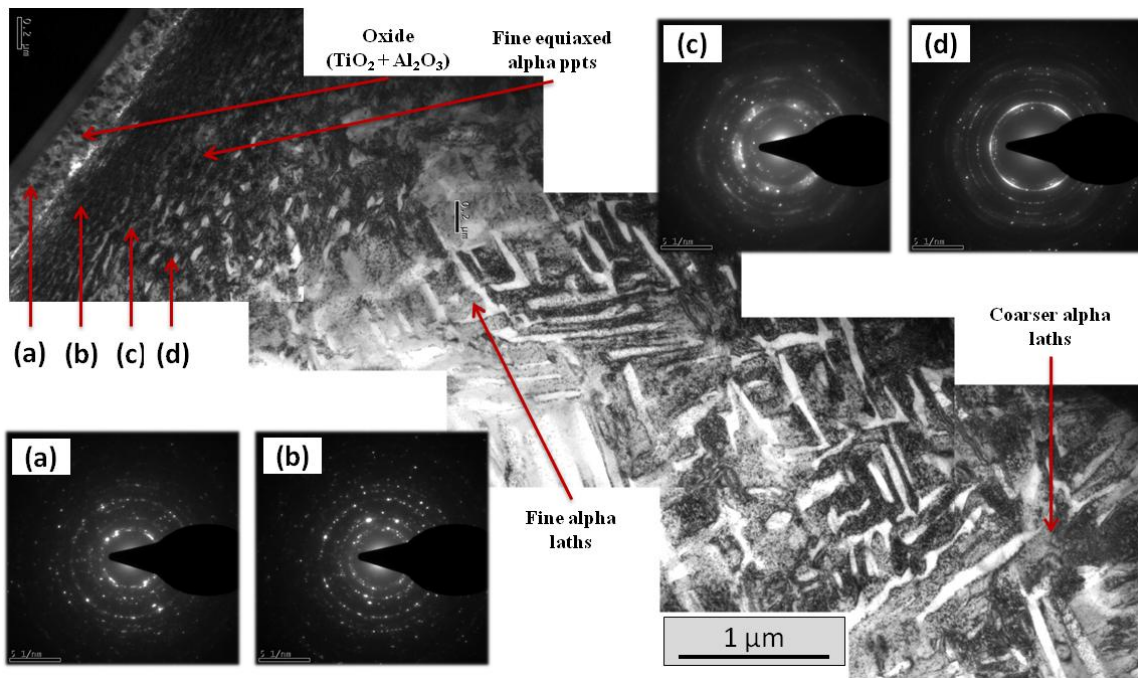
Figure 36: Bright field TEM montage showing transition from oxide layer (left edge) to bulk matrix (right edge) along with diffraction patterns from specific regions as marked by (a-d)

Figure 37(a) and (b) show x-ray diffraction patterns obtained from bulk matrix of the alloy and the oxide surface respectively. In Figure 37(a), the intensity peaks for α and β phases could be clearly identified while in Figure 37(b), the diffraction pattern from the oxide surface, in addition to α and β phases showed peaks corresponding to rutile (TiO_2). The scans were intentionally conducted in Bragg Brentano setup mode to include intensity peaks from subsurface layers beneath the oxide. On careful comparison between the bulk and oxide patterns one can note the relative shift of intensity peaks for both α and β phases due to oxidation, as shown by dotted lines in Figure 37. In comparison to the bulk matrix, intensity maxima's for α phase in the oxide surface seem to be shifted towards lower 2-theta angles. This could be due to oxygen dissolution in the subsurface layers that leads to an increase in the lattice parameter of α phase, by occupying a fraction of the octahedral interstitial sites. In contrast, intensity peaks for β phase seem to shift towards higher 2-theta angles in the x-ray diffraction plot of the oxide surface. This shift may be interpreted in a way that during the

66

oxidation process, oxygen a α stabilizer, drives towards precipitation of fine scale α. This increases the volume fraction of α, consequently enriching the β phase in β-stabilizing alloying elements like Mo. Since, Mo has a smaller atomic radius than Ti, an increased amount of it results in a decrease of β phase lattice parameter, thus shifting the corresponding peaks to higher 2-theta values. The solubility of Mo in α phase also decreases with increase in its oxygen content, leading to increase in the lattice parameter. The lattice parameter changes, as tabulated in Figure 37 itself, clearly shows that oxygen ingress in α phase results in an increase of both 'a' and 'c' lattice parameters. However the lattice parameter in the 'c' direction increases to a larger extent, thus increasing the c/a ratio, as observed in other synchrotron based studies [41]. A difference in the angular shift is observed for different peaks of α phase. The shift in case of [0002] peak of α phase is seen to be markedly more than the shift for [10-10]α peak. Similarly, the peak shift for [10-12]α is more than [11-20]α. Thus it can be concluded that angular shifts of peak intensities is higher for basal and pyramidal planes compared to prismatic planes. The increase in lattice parameter in the 'c' direction is greater than those in 'a' or 'c+a' directions. This could be due to the interstitial oxygen atoms that occupy the octahedral sites of HCP α, resulting in a non-uniform change in lattice parameters (c and a values).
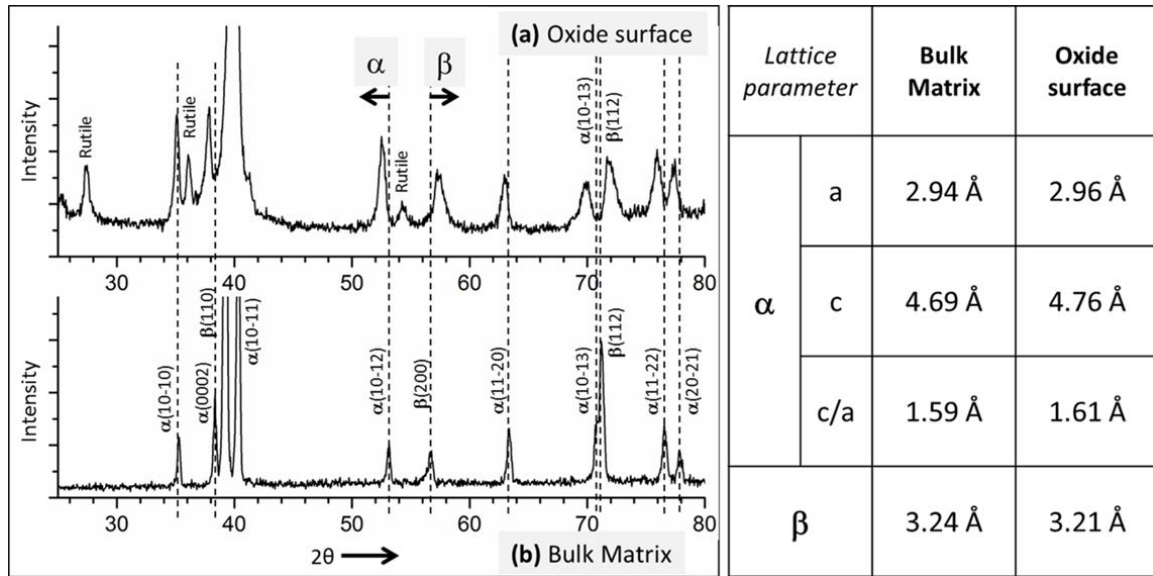
Figure 37: X-Ray diffraction patterns (Intensity versus 2theta) of (a) Oxide surface and (b) bulk matrix of oxidized Beta 21S. Associated table shows the calculated lattice parameter values for α and β phases.

The variation of lattice parameter for α-Ti with oxygen content has been previously reported in literature [6], [42]. The pronounced increase in lattice parameter in the 'c' direction is also noted. The lattice parameter of α-Ti in the 'c' direction increases from 4.68Å to 4.82Å with an increase in oxygen content from 0 to 40at%. With reference to the above mentioned tabulated values (Figure 37), in the present study an oxygen content of about 20-25 at% could be estimated in the oxygen enriched α case layer, underneath the oxide layer. The variation of lattice parameter for β-Ti phase with Mo content, has been previously reported in case of the Beta III (Ti-11.5Mo-6Zr-4.5Sn wt%) alloy [6]. The β lattice parameter was shown to decrease by about 0.02Å for a 6 wt% increase in the Mo concentration in the β phase. In the present study, the observed β phase lattice parameter decrease of 0.03Å after oxidation can therefore be attributed to a Mo enrichment of approximately 8 wt%.

In order to confirm the compositional variations in the oxygen enriched region, atom probe studies were performed on site-specific lift-out samples to compare the compositional

partitioning between α and β phases. Two sites which were chosen are shown in Figure 38. The first lift-out was taken from a region in the oxygen enriched case layer at a distance of 5μm from the oxide layer/case layer interface as shown in Figure 38(a). APT specimens were prepared from the region marked by the rectangle. Inset in the figure shows micrograph during the process of the specimen preparation. The region of interest is protected by a protective layer of platinum. The second lift-out was taken from a region (platinum deposited bright region) in the bulk matrix as shown in Figure 38(b).
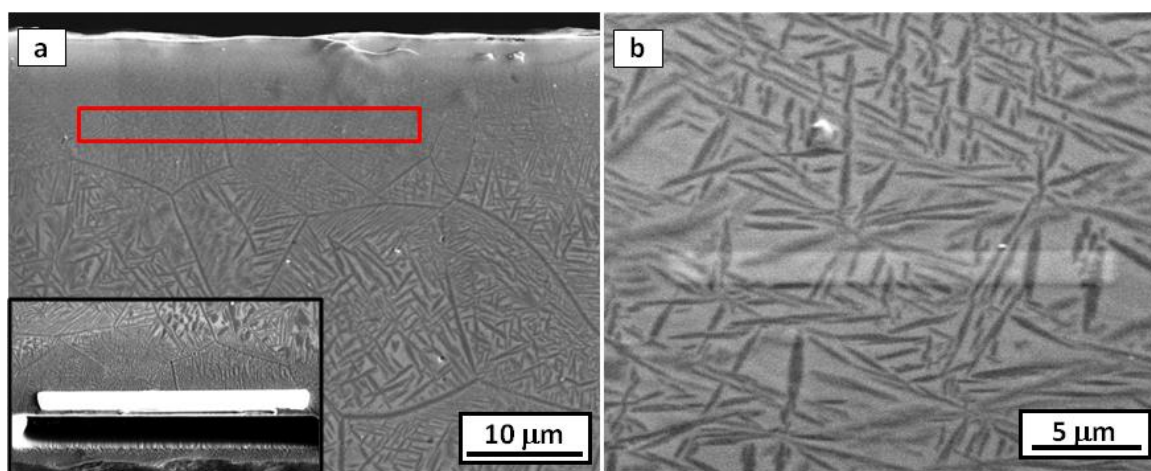
Figure 38: Sites for APT samples (a) 5μm from the oxide-alloy interface, inset shows the protective platinum coating along with trench on one side (b) in the bulk matrix

Figure 39 shows proximity histograms depicting compositional partitioning averaged over the entire α/β interface, along with the actual 3D reconstructed volume, exhibiting the α and β phases corresponding to the two above mentioned sites. These plots show molybdenum enrichment (from 15 at% to 19 at%) in the β phase of the oxygen enriched case layer (shown in Figure 39(b)) when compared with the β phase in the bulk matrix (shown in Figure 39(a)). This could be presumably due to a lower volume fraction of the β-phase in the case layer as discussed. Figure 39(b) also shows higher oxygen concentration (8 at%) in the α phase of the fine scale alpha precipitated region within the case layer, which is in qualitative agreement

with the predictions afforded by the lattice parameter measurements from x-ray diffraction, discussed previously. The slight difference between the oxygen concentration values calculated from the lattice parameter measurements versus those measured directly from the atom probe experiments can be rationalized based on the fact that the atom probe studies correspond to samples extracted at a distance of 5μm from the oxide-case layer interface, while the x-ray diffraction results correspond to an average α lattice parameter very near to the same interface (within ~1 μm). Consequently the measured oxygen concentration in α from the atom probe results is a little lower than those calculated from the x-ray diffraction lattice parameters. Another interesting observation made in the APT reconstructions was the pileup of silicon at the α/β interface. Silicon has been seen to not favor either of the phases present but rather pileup at their interface upon long term aging. This has been seen for all cases with high volume fraction of α in the β matrix including in this case, the bulk alloy and case layer.
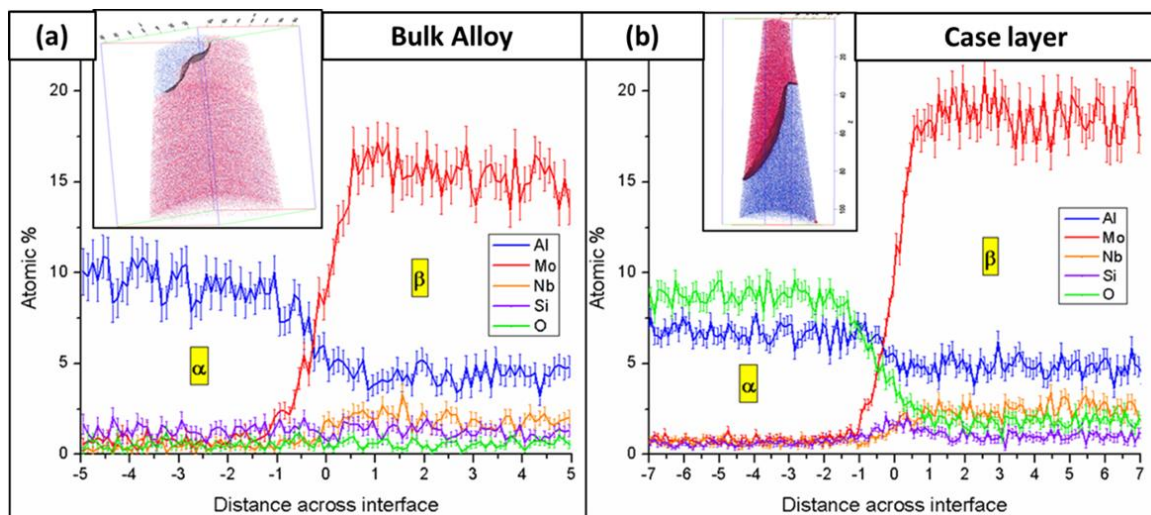
Figure 39: Proximity histograms, using 3D-Atom Probe, showing compositional partitioning between α and β phases for specimens from two different sites; (a) Bulk matrix (b) Oxygen enriched case layer region, at a depth of 5μm from the oxide-alloy interface. The ion maps for the reconstructed sample volume have also been shown for respective cases. Red dots – Molybdenum and Blue dots – Aluminum ions. The vertical bars on top of each plot signify the associated statistical error with each measurement.

In this study, the influence of oxygen diffusion on the microstructure and hardness of oxide and oxygen-enriched regions in an oxidized β-Ti alloy has been investigated. Overall the experimental observations can be summarized as follows:

i. Oxidation of β solutionized and water quenched samples of Beta 21S, leads to fine scale α precipitation next to the oxide layer (layer 1). The oxygen enriched case layer right below the oxide layer comprises of a two-phase mixture of rutile (TiO_2) and fine scale equiaxed α grains (layer 2).

ii. With further increase in depth, due to oxygen ingress, a substantial gradient in α size scale and nucleation density can be observed, starting with fine scale lath-like α (layer 3) which slowly transitions into coarser α laths (layer 4) in the bulk matrix. The observed microstructural changes could be directly attributed to the presence of oxygen gradient, as confirmed by EPMA and SEM-EDS studies.

iii. Within the oxygen-enriched layer, there is an increase in the lattice parameters of α phase as well as the 'c/a' ratio. In contrast, the lattice parameter of β phase within the same region decreases due to the enrichment of Mo and Nb, elements that have smaller atomic radii than Ti.

iv. Atom probe studies show quantitatively the enrichment of Mo in the β phase and oxygen in α phase, within the oxygen enriched α case layer close to the oxide layer. Oxygen being a α stabilizer, almost entirely partitions to the α phase as evident from these observations. The observed enrichment in Mo and oxygen concentrations matches quite well with estimated values mentioned in the previously published literature.

v. The microstructural changes appear to have a significant influence on the mechanical properties of these layers, as evident from nano-indentation results.

5.5. Conclusions

Based on these experimental observations, possible mechanisms influencing α precipitation due to the ingress of oxygen during oxidation of Beta 21S can be postulated. In addition to oxygen ingress, formation of a mixed two-phase region consisting of α + TiO$_2$ (Rutile) right next to the oxide layer, where the α precipitates tend to exhibit a near-equiaxed morphology, is also noted. This ingress of oxygen, a α stabilizer, creates a concentration gradient of it across the oxide-alloy interface which consequently results in a systematically decreasing β transus temperature from the region adjacent to the oxide layer into the bulk alloy. Effect of oxygen on β transus temperature for alloys such as Ti-6Al-4V has previously been shown by researchers [6]. Furthermore, it should be noted that the β transus temperature could be substantially higher than the bulk at regions closer to the oxide layer. This gradient in the local β transus temperature leads to a systematically changing undercooling with the regions adjacent to the oxide layer experiencing the highest undercooling for a constant overall annealing temperature (650°C in this case). Consequently, based on classical nucleation theory the α nucleation rate and spatial density will be much higher in the oxygen-enriched region leading to finer scale precipitates. Additionally, the possible clustering of oxygen or complexes such as carbon-oxygen atoms within the β matrix can potentially act as α nucleation sites as discussed by others [43], [44]. However, such clustering has not yet been directly experimentally verified and needs further investigation.

CHAPTER 6

SUMMARY AND INFERENCES

The present work aimed at improving the understanding of different precipitation mechanisms to engineer homogeneously distributed fine size scale α precipitation in β-Ti alloys, focusing on Beta 21S alloy. The work involved understanding various non-classical precipitation mechanisms for α precipitation. These mechanism in some cases involved presence of heterogeneous nucleation sites in form of metastable phases or interstitial additions. In other cases the mechanism involved direct precipitation from the β phase. The entire work was categorized into three broad sections.

The first section focused on understanding the influence of prior low temperature aging on the α precipitation behavior. The structural and compositional evolution of the metastable intermediate phase, ω phase on extended aging at low temperatures was determined. Omega precipitates were found to be essentially titanium rich pockets. The structure and composition of alpha phase growing close to these omega precipitates was also identified. The influence of the chosen aging temperature, for the two step aging treatment, on α precipitation was also understood. The precipitation sequence upon long term isothermal aging above the ω solvus temperature was studied. Extremely fine α precipitate with non equilibrium composition was found to precipitate initially. It was also found that Al, traditionally known as α stabilizers, had no tendency to partition towards well formed α laths at 400°C.

Homogeneous precipitation of α phase directly from the β matrix, without the influence of any heterogeneous nucleation sites was shown to occur upon step quenching heat treatments for Beta 21S alloy. The observations along with other analysis was shown to

73

match up with the previously proposed "pseudo-spinodal decomposition mechanism' for α precipitation in β titanium alloys.

The influence of interstitial oxygen on α precipitation during oxidation of Beta 21S alloy was studied using multiple characterization techniques. The variation of microstructure and mechanical properties with depth of oxygen ingress was calculated. A gradient in size scale of α precipitates was observed corresponding to gradient in oxygen concentration. The effect of oxidation on lattice parameters of α and β phases close to the oxide layer was calculated. These changes in lattice parameters were correlated theoretically to compositional changes in the respective phases based on existing literature data. Subsequently, these compositional changes were also verified using Atom probe tomography techniques, which showed the ingress of oxygen into α phase.

REFERENCES

[1]   L. Christoph and P. Manfred, *Titanium and Titanium Alloys*. John Wiley & Sons, 2006, p. 532.

[2]   T. Duerig and J. Williams, "Overview: microstructure and properties of beta titanium alloys," *Beta Titanium Alloys in the 1980's*, 1983.

[3]   D. A. Porter and K. E. Easterling, *Phase transformations in metals and alloys*. Stanley Thornes, 1992, p. 514.

[4]   D. de Fontaine, N. E. Paton, and J. C. Williams, "The omega phase transformation in Titanium alloys as an example of displacement controlled reactions," *Acta Metall. (USA)*, vol. 19, no. 11, pp. 1153 – 62.

[5]   T. W. Duerig, G. T. Terlinde, and J. C. Williams, "Omega phase reaction in titanium alloys.," 1980, vol. 2, pp. 1130–1299.

[6]   R. Boyer, G. Welsch, and E. W. Collings, *Materials properties handbook: Titanium alloys*. Materials Park, OH: ASM International, 1994.

[7]   S. Nag, *Influence of beta instabilities on the early stages of nucleation and growth of alpha in beta titanium alloys*. 2008.

[8]   D. Eylon, R. R. Boyer, and D. A. Koss, "Applications of Beta Titanium Alloys in Airframes, Beta Titanium Alloys in the 1990's," *The Materials Society*, pp. 335–346, 1993.

[9]   P. J. Bania and W. M. Parris, "Beta 21S: A high temperature metastable beta titanium alloy," in *Proceedings of the 1990 international conference on titanium products and applications*, 1990, pp. 784–793.

[10]   J. C. Fanning, "Timetal 21S Property data," in *Beta titanium alloys in the 1990's*, 1993, pp. 397–410.

[11]   K. Chaudhuri and J. H. Perepezko, "Microstructural study of the titanium alloy Ti-15Mo-2.7Nb-3Al-0.2Si (TIMETAL 21S)" *Metallurgical and Materials Transactions A*, vol. 25A, no. June, p. 1109, 1994.

[12]   M. K. Miller, K. F. Russell, K. Thompson, R. Alvis, and D. J. Larson, "Review of atom probe FIB-based specimen preparation methods.," *Microscopy and microanalysis : the official journal of Microscopy Society of America, Microbeam Analysis Society, Microscopical Society of Canada*, vol. 13, no. 6, pp. 428–36, Dec. 2007.

[13]   M. K. Miller, *Atom Probe Tomography: Analysis at the Atomic Level*. New York: Kluwer Academic/Plenum publishers, 2000.

[14] M. K. Miller, "Contributions of atom probe tomography to the understanding of nickel-based superalloys q," *Science*, vol. 32, no. 2001, pp. 757–764, 2008.

[15] M. J. Blackburn and J. C. Williams, "Phase Transformation in Ti-Mo and Ti-V Alloys," *Trans TMS-AIME*, vol. 242, pp. 2461–2469, 1968.

[16] A. Vassel, "Microstructural Instabilities in Beta Titanium Alloys," *Beta titanium alloys in the 1990's*, pp. 173–185, 1990.

[17] S. Nag, R. Banerjee, R. Srinivasan, J. Y. Hwang, M. Harper, and H. L. Fraser, "ω-Assisted nucleation and growth of α precipitates in the Ti–5Al–5Mo–5V–3Cr–0.5Fe β titanium alloy," *Acta Materialia*, vol. 57, no. 7, pp. 2136–2147, Apr. 2009.

[18] F. Prima, P. Vermaut, G. Texier, D. Ansel, and T. Gloriant, "Evidence of α-nanophase heterogeneous nucleation from ω particles in a β-metastable Ti-based alloy by high-resolution electron microscopy," *Scripta Materialia*, vol. 54, no. 4, pp. 645–648, Feb. 2006.

[19] W. JC and B. MJ, "INFLUENCE OF MISFIT ON THE MORPHOLOGY AND STABILITY OF THE OMEGA PHASE IN TITANIUM-TRANSITION METAL ALLOYS," vol. 245, no. 10, pp. 2352–2355, 1969.

[20] G. M. Pennock, H. M. Flower, and D. R. F. West, "Control of alpha precipitation by two step ageing in beta Ti-15%Mo.," 1980, vol. 2, pp. 1135–1343.

[21] S. Azimzadeh and H. J. Rack, "Phase transformations in Ti-6.8Mo-4.5Fe-1.5Al," *Metallurgical and Materials Transactions A: Physical Metallurgy and Materials Science*, vol. 29 A, no. 10, pp. 2455–2467, 1998.

[22] T. Gloriant, G. Texier, F. Sun, I. Thibon, F. Prima, and J. L. Soubeyroux, "Characterization of nanophase precipitation in a metastable β titanium-based alloy by electrical resistivity, dilatometry and neutron diffraction," *Scripta Materialia*, vol. 58, no. 4, pp. 271–274, Feb. 2008.

[23] E. Lee, R. Banerjee, and S. Kar, "Selection of α variants during microstructural evolution in α/β titanium alloys," *Philosophical Magazine*, Vol 87, Issue 24, pp. 3615-3627, 2007.

[24] S. C. Wang, M. Aindow, and M. J. Starink, "Effect of self-accommodation on α/α boundary populations in pure titanium," *Acta Materialia*, vol. 51, no. 9, pp. 2485–2503, May 2003.

[25] W. F. Miao and D. E. Laughlin, "Precipitation hardening in aluminum alloy 6022," *Scripta Materialia*, vol. 40, no. 7, pp. 873–878, 1999.

[26] A. K. Jena and M. C. Chaturvedi, "The role of alloying elements in the design of nickel-base superalloys," *Journal of Materials Science*, vol. 19, no. 10, pp. 3121–3139, Oct. 1984.

[27] A. M. Mebed and T. Miyazaki, "Computer simulation and experimental investigation of the spinodal decomposition in the β Ti-Cr binary alloy system," *Metallurgical and Materials Transactions A*, vol. 29, no. 3, pp. 739–749, Mar. 1998.

[28] H. P. Ng, A. Devaraj, S. Nag, C. J. Bettles, M. Gibson, and H. L. Fraser, "Phase separation and formation of omega phase in the beta matrix of a Ti – V – Cu alloy," *Acta Materialia*, vol. 59, pp. 2981–2991, 2011.

[29] S. Nag, Y. Zheng, R. E. A. Williams, A. Devaraj, A. Boyne, Y. Wang, P. C. Collins, G. B. Viswanathan, J. S. Tiley, B. C. Muddle, R. Banerjee, and H. L. Fraser, "Non-classical homogeneous precipitation mediated by compositional fluctuations in titanium alloys," *Acta Materialia*, vol. 60, no. 18, pp. 6247–6256, Oct. 2012.

[30] Y. Ni and A. G. Khachaturyan, "From chessboard tweed to chessboard nanowire structure during pseudospinodal decomposition.," *Nature materials*, vol. 8, no. 5, pp. 410–4, May 2009.

[31] *Advanced aerospace alloys*. Materials engineering, p. 26.

[32] R. R. Boyer, "An overview on the use of titanium in the aerospace industry," *Materials Science and Engineering: A*, vol. 213, no. 1–2, pp. 103–114.

[33] J. Fanning and S. Fox, "Recent developments in metastable β strip alloys," *Journal of materials engineering and performance*, Vol 14, Issue 6, pp. 703-708, Dec 2005.

[34] R. Schutz, "Environmental behavior of beta titanium alloys," *JOM - Journal of the Minerals, Metals and Materials,* Vol 46, Issue 7, pp.24-29, July 1994.

[35] N. Agarwal and A. Bhattacharjee, "Heat treatment, microstructure and mechanical properties of a metastable β titanium alloy timetal® 21s," *Transactions of the Indian Institute of Metals*, vol. 61, no. 5, pp. 419–425, 2008.

[36] X. Huang, J. Cuddy, N. Goel, and N. Richards, "Effect of heat treatment on the microstructure of a metastable beta-titanium alloy," *Journal of materials science*, vol. 3, no. 4, pp. 560–566, 1994.

[37] X. Guangjun, Y. Gaiying, and Z. Jing, "Oxidation behavior of beta 21S titanium alloy over temperature range 600 C to 800 C," *Rare metals*, vol. 18, no. 3, Sep 1999.

[38] T. A. Wallace, R. K. Clark, and K. E. Wiedemann, "Oxidation characteristics of Beta 21s in air in the temperature range 600C to 800C," *NASA Technical memorandum*, March, 1992.

[39] A. M. Chaze and C. Coddet, "Influence of alloying elements on the dissolution of oxygen in the metallic phase during the oxidation of titanium alloys," *Journal of materials science*, vol. 22, pp. 1206–1214, 1987.

[40] F. Sansoz, M. Almesallmy, and H. Ghonem, "Ductility exhaustion mechanisms in thermally exposed thin sheets of a near-β titanium alloy," *Metallurgical and Materials*, vol. 35A, pp. 3113, Oct 2004.

[41] S. Malinov, W. Sha, Z. Guo, C. . Tang, and a. . Long, "Synchrotron X-ray diffraction study of the phase transformations in titanium alloys," *Materials Characterization*, vol. 48, no. 4, pp. 279–295, Jun. 2002.

[42] R. J. Van Thyne, E. S. Bumps, H. D. Kessler, and M. Hansen, "*Phase diagram of Titanium Aluminum, Titanium-Chromium-Iron and Titanium-Oxygen alloy systems*"

[43] Y. G. Li, P. A. Blenkinsop, M. H. Loretto, D. Rugg, and W. Voice, "Effect of carbon and oxygen on microstructure and mechanical properties of Ti-25V-15Cr-2Al alloys" *Acta Materialia*, vol. 47, no. 10, pp. 2889–2905, 1999.

[44] M. A. Imam and C. R. Feng, "Role of oxygen on transformation kinetics in Timetal-21S titanium alloy," *Advances in the Science and Technology of Titanium Alloy*, pp. 435–450, 1996.